DEPARTMENT OF PHYSICS, UNIVERSITY OF JYVÄSKYLÄ
RESEARCH REPORT No. 1/1999

CONSTRAINTS FROM HADRON SPECTRA ON THERMAL ELECTROMAGNETIC EMISSION IN HEAVY-ION COLLISIONS AT THE CERN SPS

BY
PASI HUOVINEN

Academic Dissertation
for the Degree of
Doctor of Philosophy

Jyväskylä, Finland
May 1999

URN:ISBN:978-951-39-9494-5
ISBN 978-951-39-9494-5 (PDF)
ISSN 0075-465X

Jyväskylän yliopisto, 2023

ISBN 951-39-0468-7
ISSN 0075-465X

DEPARTMENT OF PHYSICS, UNIVERSITY OF JYVÄSKYLÄ
RESEARCH REPORT No. 1/1999

CONSTRAINTS FROM HADRON SPECTRA ON THERMAL ELECTROMAGNETIC EMISSION IN HEAVY-ION COLLISIONS AT THE CERN SPS

BY
PASI HUOVINEN

Academic Dissertation
for the Degree of
Doctor of Philosophy

To be presented, by permission of the
Faculty of Mathematics and Science
of the University of Jyväskylä,
for public examination in Auditorium FYS 1 of the
University of Jyväskylä on June 4, 1999,
at 12 o'clock noon

Jyväskylä, Finland
May 1999

Preface

The work reviewed in this thesis has been carried out during the years 1994–1998 at the Department of Physics in the University of Jyväskylä.

First of all I want to thank my supervisor Prof. Vesa Ruuskanen for competent guidance and introducing me to the complicated and challenging field of heavy-ion physics. I am indebted to all my collaborators who have made it possible for me to accomplish this thesis in its present form. Especially I want to express my gratitude to Prof. M. Prakash for rekindling my inspiration and interest in physics when it was almost gone. I am also grateful to Dr. Josef Sollfrank for his advice and solutions to numerous problems and to Dr. Kari J. Eskola for continuous encouragement during the last year.

I want to thank the staff of the Department of Physics for very pleasant and inspiring atmosphere. The department has been an excellent place to work.

The financial support from the Academy of Finland, the Graduate School of Particle and Nuclear Physics and the University of Jyväskylä is gratefully acknowledged.

Finally, I want to thank my friends and my family for their support.

Jyväskylä, May 1999

Pasi Huovinen

Abstract

In this thesis the space-time evolution of matter produced in an ultrarelativistic heavy-ion collision is studied using a one-fluid hydrodynamical model. The initial state of the evolution is constrained to reproduce the observed hadron spectra in S+Au and Pb+Pb collisions at the CERN-SPS energy. Simultaneously the photon and electron pair emission are calculated and their dependence on an equation of state (EoS) and initial density distribution are studied.

The initial state of a hydrodynamic evolution is difficult to determine. To reduce the arbitrariness of choosing the initial conditions for different collisions, a parametrisation of the initial state based on baryon stopping in terms of the thickness of colliding nuclei was developed. This parametrization is applicable to all nucleus-nucleus collisions measured at the CERN SPS. With only a few parameters the main features of the hadronic spectra can be reproduced in all of them.

If the evolution is constrained to reproduce the observed hadronic spectra, the remaining freedom in the equation of state and initial distributions affects different electromagnetic observables in different ways. The photon yield depends clearly on the phase transition temperature but is sensitive to the maximum temperature only at very high values of p_T. Intermediate mass lepton pairs reflect the maximum value of temperature during the evolution and are therefore much more sensitive to the initial distributions than to the EoS. On the other hand the mass spectrum of low mass electron pairs is almost insensitive to both EoS and initial state but the shape of electron pair rapidity spectrum depends strongly on the flow and therefore on the EoS.

List of publications

This thesis consists of an introductory part and of the following publications:

I **Hydrodynamical description of 200A GeV/c S+Au collisions: Hadron and electromagnetic spectra**
J. Sollfrank, P. Huovinen, M. Kataja, P.V. Ruuskanen, M. Prakash and R. Venugopalan
Phys. Rev. C **55**, 392 (1997).
https://doi.org/10.1103/PhysRevC.55.392

II **Initial conditions in the one-fluid hydrodynamical description of ultra-relativistic nuclear collisions**
J. Sollfrank, P. Huovinen and P.V. Ruuskanen
Heavy Ion Physics **5**, 321 (1997).
https://doi.org/10.1007/BF03156108

III **Mass number scaling in ultra-relativistic nuclear collisions from a hydrodynamical approach**
J. Sollfrank, P. Huovinen and P.V. Ruuskanen
Eur. Phys. J. C **6**, 525 (1999).
https://doi.org/10.1007/s100529800934

IV **Sensitivity of electromagnetic spectra to equation of state and initial energy density in the Pb+Pb collisions at SPS**
P. Huovinen, P.V. Ruuskanen and J. Sollfrank
Nucl. Phys. **A650**, 227 (1999).
https://doi.org/10.1016/S0375-9474(99)00107-4

The author of this thesis has written the paper IV and participated in the writing of the papers I–III. The author has given a significant contribution to the development of the programs used for the numerical calculations in all the papers and has formulated one of the main ideas of the parametrisation presented in the papers II and III. The author has performed all the numerical work of the paper IV and participated in the interpretation of the results in all the papers.

Contents

Chapter 1

Introduction

One of the most intriguing predictions of the present theory of strong interaction, quantum chromodynamics (QCD), is that at sufficiently high temperatures and/or densities the fundamental constituents of matter, quarks and gluons, would no longer be confined to hadrons but move freely in this hot, dense region [1]. Analogously to atomic plasma where atoms have dissolved into electrons and nuclei, this new state of matter is usually called quark-gluon plasma, or QGP for short. Since in this phase the properties of the matter are dictated by the quark and gluon degrees of freedom, the name quark matter is also used.

The numerical simulations of QCD on lattice predict that at zero net baryon density the sufficient temperature for this deconfinement transition from hadronic phase to quark-gluon plasma phase would be 100–200 MeV [2]. The corresponding energy density depends of course on the actual equation of state, but it can be approximated to be of the order of few GeV/fm^3. In the nature so large densities are rare. In the very early universe the density and temperature could have been high enough for QGP until the universe was less than 10^{-6} seconds old [3]. In the present universe, density may be large enough for a transition to cold quark matter in a core of a large neutron star [4].

Because of the huge densities involved it is clear that it is not possible to produce large, stable amounts of quark matter. However, for a transient moment, it seems to be possible to attain sufficiently high densities in ultrarelativistic collisions of heavy ions. At present, heavy-ion experiments dedicated to probing the QCD phase diagram close to the phase transition are done at the Brookhaven AGS at $11A$ GeV and at the CERN SPS at $\approx 200A$ GeV beam energy. At the moment it is still uncertain whether QGP has been formed in Pb+Pb collisions at the CERN SPS or not. In the near future new colliders will be taken into use increasing the available energy up to $\sqrt{s} = 200A$ GeV in RHIC at Brookhaven and $\sqrt{s} = 5.5A$ TeV in the LHC/ALICE at CERN. Estimates for energy densities and temperatures achievable in RHIC and the LHC are well above the phase transition temperature [5] and, if QGP can be formed in a heavy-ion collision, it should be formed at the latest in those experiments.

The standard scenario for an ultrarelativistic nucleus-nucleus collision is that

typically around 1 fm/c after the collision, a state of deconfined quarks and gluons is formed. The immense pressure within this region starts to blow it apart and the plasma will expand and cool until it reaches the phase transition temperature T_c. At this temperature the plasma begins to rehadronise forming a mixed phase of hadrons and plasma until all the quarks and gluons have formed their bound states i.e. hadrons. After hadronisation the hadrons continue to interact forming a phase of hadron gas until, due to continuous expansion, the system is so cool and dilute that the hadrons cease to interact and fly away to the detectors.

Thus, what one observes are the hadrons basically emitted at the spacetime surface of the dense region. Due to many rescatterings the hadrons have approximately thermalised and "lost their memory" of the properties of the region they were formed in. The hadrons can therefore yield information only about this final stage of the collision, not about the earlier stages. Reproducing the hadron spectra does not necessarily mean the evolution leading to the final stage is reasonable and more information is needed to distinguish between different evolution scenarios. The advantage of electromagnetic observables, i.e. real photons and lepton pairs from virtual photons, is that their mean free paths are longer than the size of the hot and dense region and after being formed, they escape without rescattering. Therefore they carry information of the entire evolution, not only of the final stage, and are thus observables which may help to distinguish between different evolution scenarios which reproduce the final state.

To be able to study the dynamics of the collision and connect different observables one needs a model to describe the evolution of the system. Since the description of interactions between hadrons from first principles is not within our reach, all models available are more or less phenomenological. In parton cascade models the collision is described in terms of the partonic structure of the nucleons and the interactions are described using perturbative QCD which applicability at the present collision energy, $\sqrt{s} \approx 20A$ GeV, is questionable. Also the process of rehadronisation is highly nonperturbative and has to be modelled separately. Hadronic transport models like RQMD treat the collision as a sequence of collisions of mesons, baryons and their constituents where the interaction has a model dependent phenomenological form. The partonic degrees of freedom are not treated explicitly in these models and therefore these models do not include a phase transition. In the hydrodynamical models the system is assumed to be so close to local thermal and chemical equilibrium that its description in terms of hydrodynamics is feasible. This allows an explicit study of the equation of state since it is a direct input of a hydrodynamical calculation.

The main part of this thesis consists of four publications [I–IV], which were completed during the years 1996–1998. In these publications ultrarelativistic heavy-ion collisions at the CERN SPS energies have been studied using a hydrodynamical model. The main idea has been to constrain the evolution of the system to reproduce the observable single particle hadronic spectra and to study what restrictions this imposes on electromagnetic observables, i.e. photons

and lepton pairs. In the first paper [I] the model and calculation methods are explained in detail and S+Au collision at 200A GeV beam energy is studied using four different equations of state. In the following two papers [II,III] a new parametrisation for the initial state of the hydrodynamical evolution is developed. This parametrisation reduces the arbitrariness of choosing the initial state and it is shown to work in various different collisions at SPS energy. Finally, in the last paper [IV], the resolving power of electromagnetic observables to differentiate between different initial conditions and equations of state are studied in the case of Pb+Pb collision at 158A GeV beam energy.

In the following chapters I review the main ideas and conclusions of these publications. In chapter 2 the hydrodynamical model and the parametrisation of the initial state are presented. Also a sample of hadron spectra are shown to justify the use of the parametrisation. In chapter 3 the calculated electromagnetic spectra are shown and discussed and chapter 4 gives a short summary and outlook on the use of hydrodynamical models in the future.

Chapter 2

Hydrodynamical description of ultrarelativistic heavy-ion collision

The hydrodynamical modelling of heavy ion collisions has a long history dating back to the fifties [6]. When applicable, hydrodynamics has some advantages over the more fundamental kinetic calculations. Besides its relative simplicity, the use of familiar concepts like temperature, flow velocity, energy and baryon density, temperature etc., leads to an intuitively transparent picture of the evolution of the hot and dense stage of the collision. Another great advantage is the direct use of the equation of state of strongly interacting matter. This enables one to test different phase transition scenarios explicitly without the need to know the complicated deconfinement and hadronisation processes in detail. Also it is important to keep in mind that it is meaningful to talk about plasma formation in a heavy-ion collision only if the matter has enough time to reach thermal equilibrium and form a thermal system. Thus, if the plasma is formed, at least the gross details of its behaviour have to be describable using a thermodynamical model.

Basically, relativistic hydrodynamics is nothing more than an application of conservation laws. The basic equations of hydrodynamics are the local conservation of energy and momentum, which in covariant form take the deceivingly simple form

$$\partial_\mu T^{\mu\nu}(x) = 0. \tag{2.1}$$

If there are other conserved quantities $j_i(x)$ in addition to energy and momentum, there is an equivalent local conservation equation of the form

$$\partial_\mu j_i^\mu = 0 \tag{2.2}$$

for each of them. In this thesis finite baryon density is taken into account. Local baryon conservation necessitates thus an equation of the form 2.2, where j_i is the baryon four-current $J_B^\mu = \rho_B u^\mu$ and ρ_B is baryon density in a comoving frame.

In the ideal fluid approximation used in this thesis the energy-momentum tensor $T^{\mu\nu}$ has the form

$$T^{\mu\nu} = (\epsilon + p)u^\mu u^\nu - g^{\mu\nu}p, \tag{2.3}$$

where u^μ is the flow four-velocity and ϵ and p are the energy density and pressure measured in the comoving frame of the fluid, respectively. In the ideal fluid approximation dissipative and viscous effects are assumed to be negligible. In principle these effects could be included but this would lead to a major increase in complexity and computational effort. So far no serious attempts have been made to describe heavy-ion collisions using relativistic hydrodynamics with viscous effects [7].

The equations (2.1) and (2.2) do not form a closed set but have to be supplemented by a further constraint to be solved. This is done by specifying an equation of state (EoS),

$$p = p(\epsilon, \rho_B), \tag{2.4}$$

which gives pressure in terms of energy and baryon density. The eqs. (2.1) and (2.2) are independent of the properties of the particle fluid and all the microscopic dynamics is included in the equation of state.

When the equation of state and the initial conditions are specified, the evolution of the system is dictated by the continuity equations and one may solve the densities and flow velocity as a function of time and position. When the system expands and cools down, the mean free paths increase until they exceed the size of the system. At that time the hydrodynamical description is no longer applicable. The particles cease to interact and behave as free streaming particles instead.

The hydrodynamical approach is conceptually simple and feasible. The numerical solution of eqs. (2.1) and (2.2) allows one to calculate various experimental observables like hadron transverse momentum and rapidity distributions and photon and dilepton production. The model has, however, some important limitations. At ultrarelativistic energies the primary collisions can not be described using hydrodynamics but have to be modelled separately (see section 2.3). By definition the model does not describe how and whether the particles produced in primary collisions evolve towards thermalisation nor what kind of particles are emitted during that time. Hydrodynamics is also a deterministic approach which means that the event to event fluctuations are absent. To certain extent the fluctuations can be simulated by using an ensemble of initial conditions, but the evolution itself does not produce any fluctuations. The transition from particle fluid to free-streaming particles is also nontrivial (see section 2.4).

In the following, the details of the numerical method of solving the eqs. (2.1) and (2.2) are discussed in section 2.1. Appropriate equations of state for hot and dense strongly interacting matter are discussed in section 2.2 and the problematics of choosing the initial state and the end of the evolution are discussed in sections 2.3 and 2.4, respectively.

2.1 Numerical details

Unfortunately there are no analytic solutions for the continuity equations (2.1) and (2.2) in more than one dimension and they have to be solved by other means. In this thesis the equations are solved numerically in two spatial dimensions, longitudinal and transverse, using a finite difference method. The actual algorithm employed is the FCT-SHASTA[1] algorithm by Boris and Book [8]. The application of SHASTA algorithm to 2+1 dimensions and cylindrical symmetry is by no means a new one. The numerical code used to find the solutions in this thesis is based on the code written by M. Kataja, which was first used to calculate results presented in ref. [9].

In principle SHASTA algorithm is easy to generalise to multidimensions, but in the case of cylindrical coordinates one has to pay attention to certain details to avoid violation of conservation laws. Also, if the generalisation is not done carefully, the algorithm may no longer treat steep gradients properly. To understand the difficulties connected with cylindrical coordinates, it is necessary to outline the algorithm here.

2.1.1 SHASTA-algorithm

The idea of the FCT (Flux Corrected Transport) method is to combine the best features of two different algorithms – a high-order and a low-order algorithm – by giving the final result as a weighted sum of solutions produced by the two algorithms [10,11]. In general high-order methods provide accurate solutions when the transported density profile is smoothly varying but produce erroneous short wavelength oscillations near steep gradients. These oscillations are due to numerical dispersion (i.e. different Fourier harmonics of the profile proceed at different velocities) and Gibbs phenomena (uncertainty in the profile due to representing a continuous profile at only N distinct points). On the other hand, low-order methods do not suffer from such oscillations, since strong numerical diffusion damps them down. However, this strong diffusion itself is erroneous and smooths out possible shock fronts and steep gradients.

The FCT technique circumvents these problems by applying extra diffusion to the high-order solution to prevent the formation of dispersive errors only in those regions where these errors tend to form. In practice the computation proceeds in two stages. During the first, transport stage, the low-order method is used to calculate a tentative solution $\bar{\rho}_j^{n+1}$. Then so-called antidiffusive fluxes $A_{j\pm1/2}$ are defined using the solution given by the high-order method. These fluxes correspond to the fluxes from cell j to $j+1$ due to diffusion and if they were subtracted from $\bar{\rho}_j^{n+1}$ as such, the result would be that of the high-order scheme. However, in order to avoid the formation of the dispersive ripples, these antidiffusive fluxes are corrected or limited to

$$A^c_{j+1/2} = C_{j+1/2} A_{j+1/2}, \quad 0 \leq C_{j+1/2} \leq 1, \tag{2.5}$$

[1] SHarp And Smooth Transport Algorithm

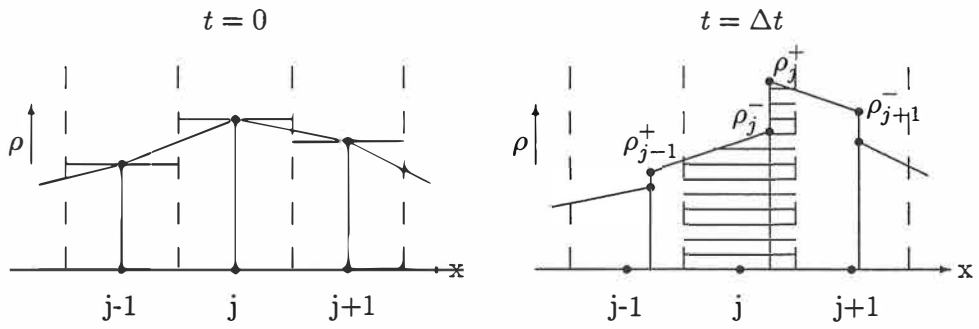

Figure 2.1: The transport stage of one-dimensional SHASTA. The shaded region depicts the amount of fluid in cell j at time Δt.

and the final values of ρ_j at the time t^{n+1} are calculated as

$$\rho_j^{n+1} = \bar{\rho}_j^{n+1} - (A^c_{j+1/2} - A^c_{j-1/2}). \tag{2.6}$$

The desired effect is achieved by correcting the flux in such a way that the final density profile, ρ^{n+1}, must not have extrema which are not present in the tentative solution, $\bar{\rho}_j^{n+1}$, or in the initial density profile, ρ_j^n. Also it is required that any flux subtracted from somewhere is added somewhere else [10].

The transport stage of SHASTA can be represented pictorially. In fig. 2.1 the density ρ is shown at different steps of one-dimensional computation. At the beginning of each timestep, the density profile is approximated by straight lines between the values of ρ at grid points (fig. 2.1, $t = 0$). The grid points are then moved to new positions $x_j + v_j \Delta t$. Since each point moves different distance, the densities at each point have to be scaled accordingly to conserve the amount of transported quantity. Resulting densities are marked as ρ_j^+ and ρ_j^- in fig. 2.1, $t = \Delta t$. Finally the new values of the density, $\bar{\rho}_j^{n+1}$, at the original grid points are computed by calculating the amount of fluid in each cell, which have not moved (the shaded area in fig. 2.1, $t = \Delta t$), and the corresponding density. This procedure leads to an equation

$$\begin{aligned} \bar{\rho}_j^{n+1} &= \frac{1}{2} Q_-^2 (\rho_{j-1}^n - \rho_j^n) + \frac{1}{2} Q_+^2 (\rho_{j+1}^n - \rho_j^n) + (Q_+ + Q_-)\rho_j^n \\ Q_\pm &= \frac{1/2 \mp \epsilon_j}{1 \pm (v_{j+1} - v_j)\frac{\Delta t}{\Delta x}}, \end{aligned} \tag{2.7}$$

where $\epsilon_j = |v_j\,(\Delta t/\Delta x)|$. The quantities Δt and Δx are the grid differences and v_j is a time centered velocity.

In SHASTA the high order solution of FCT is not explicitly stated. Instead, the antidiffusive fluxes are defined as

$$A_{j+\frac{1}{2}} = \eta(\bar{\rho}_{j+1}^{n+1} - \bar{\rho}_j^{n+1}), \tag{2.8}$$

where η is the antidiffusive coefficient. This form is obtained by demanding that in the case of constant velocity the diffusion of the transport stage is cancelled. To avoid the formation of erroneous oscillations these fluxes are limited as described in eq. (2.5) and the final value of the density is given by eq. (2.6). The procedure for calculating the appropriate values of the flux limiting factors $C_{j+1/2}$ is explained in ref. [10].

The relative weighting of the high-order and low-order solutions can be adjusted by changing the value of the antidiffusive coefficient η. Theoretically the value $\eta = 1/8$ would remove the diffusion almost completely, but it would also lead to the formation of dispersive ripples in the vicinity of steep gradients. The actual value of η has only a small effect on the final results. Therefore a slightly smaller value of η (0.11 in paper I and 0.115 in papers II–IV) has been used in this thesis to prevent the formation of these errors.

2.1.2 Generalisations for cylindrical coordinates

When the continuity equations (2.1) and (2.2) are written in cylindrical coordinates, additional geometrical terms appear. For example, the continuity equation for baryon density becomes

$$\partial_0 j^0 = -\partial_1(j^0 v^1) - \partial_2(j^0 v^2) - \frac{1}{r} j^0 v^2, \tag{2.9}$$

where the coordinates are renamed as $t \leftrightarrow 0$, $z \leftrightarrow 1$ and $r \leftrightarrow 2$. SHASTA algorithm can be used to solve equations of this type if the geometrical term $\frac{1}{r} j^0 v^2$ is treated as a source term. In this particular case the densities at time t^{n+1} are calculated as

$$\tilde{\rho}_j^{n+1} = \rho_j^{n+1} - \frac{1}{r} \rho_j v_j^2 \Delta t, \tag{2.10}$$

where ρ_j^{n+1} is defined as in eq. (2.6). ρ_j and v_j are the time centered values of density and velocity, respectively.

However, such an easy generalisation may lead to problems with conservation laws. The transport stage described above carries densities from one cell to another but the cells are not of equal size. The difference in size is corrected by the geometrical term of eq. (2.10), but these terms correct only that part of the flux which is due to flow velocity. Thus in those regions where diffusion is not completely removed, density is decreased in one cell and increased by the same amount in another cell of different size. This leads to non-conservation of the transported quantity.

This kind of solution is also prone to unphysical ripples. In the original version of SHASTA, the flux-limiting procedure prevents their formation, but if the contribution of the geometric term is added after flux-limiting, new extrema may appear.

There are basically two different ways to solve these problems. The first one is to rewrite the transport stage using actual yields transported into and from each cell instead of densities. Another method is to modify the flux-correction

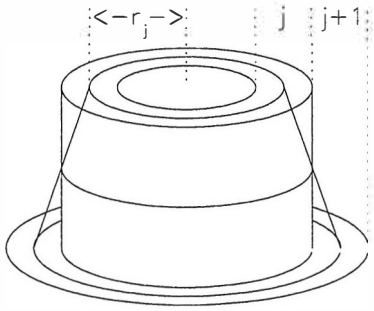

Figure 2.2: Linear approximation of the density profile in cylindrical cells.

procedure in such a way that the anti-diffusive flux is never put to zero but contains always a part large enough to compensate the change of densities due to different cell sizes. In both cases the grid point where $r = 0$ has to be treated separately. The treatment of these points is omitted in the following short descriptions.

Radial-SHASTA[2]

A straightforward way to make SHASTA algorithm to function with cylindrical coordinates is to redo the reasoning leading to eq. (2.7) for cylindrical fluid cells and use actual yields of fluid in each cell instead of fluid densities (see fig. 2.2). In this case, at zero velocity the amounts of fluid moved from cell j to cell $j+1$ and from cell $j-1$ to cell j by the linear approximation of the density profile are

$$2\pi\, r_{j\pm1/2} \cdot \frac{1}{2}\frac{\Delta r}{2}\,\frac{\rho^n_{j\pm1} - \rho^n_j}{2}. \tag{2.11}$$

Thus the density in cell j at the next time step is

$$\bar{\rho}^{n+1}_j = \rho^n_j + \frac{1}{8}\frac{r_{j-1/2}}{r_j}(\rho^n_{j-1} - \rho^n_j) + \frac{1}{8}\frac{r_{j+1/2}}{r_j}(\rho^n_{j+1} - \rho^n_j). \tag{2.12}$$

Similar reasoning for a general velocity field leads to equations

$$\begin{aligned} \bar{\rho}^{n+1}_j &= \frac{1}{2}\frac{r_{j-1/2}}{r_j}\,Q^2_-(\rho^n_{j-1} - \rho^n_j) + \frac{1}{2}\frac{r_{j+1/2}}{r_j}\,Q^2_+(\rho^n_{j+1} - \rho^n_j) + (Q^r_+ + Q^r_-)\rho^n_j \\ Q^r_\pm &= \frac{1/2 \mp \frac{r_{j\pm1/2}}{r_j}\epsilon}{1 \pm (v_{j+1} - v_j)\frac{\Delta t}{\Delta x}}, \end{aligned} \tag{2.13}$$

where $Q_\pm$ and ϵ are as in eq. (2.7). In the same way the effect of cell sizes can be incorporated in antidiffusive fluxes by defining the flux in radial direction as

$$A_{j+\frac{1}{2}} = \eta\frac{r_{j+1/2}}{r_j}(\bar{\rho}^{n+1}_{j+1} - \bar{\rho}^{n+1}_j), \tag{2.14}$$

[2]This approach has been explained in greater detail in ref. [12]

instead of eq. (2.8).

Now there is no need for the geometrical source term of the eq. (2.10). The remaining diffusive fluxes are scaled by difference in cell sizes which conserves the transported quantity and flux limiting is done for the actual fluxes which keeps it effective.

Modified flux correction

Alternative approach to rewriting the transport stage is to change only the flux-limiting stage to take into account the geometry. The approach presented here is formulated by Josef Sollfrank and major part of the calculations of this thesis are done using this method.

At zero velocity the original transport stage of SHASTA results in the following equation for the density at timestep $n+1$:

$$\bar{\rho}_j^{n+1} = \rho_j^n + \frac{1}{8}(\rho_{j+1}^n - 2\rho_j^n + \rho_{j-1}^n), \tag{2.15}$$

whereas eq. (2.13) gives for the diffusion to radial direction at zero velocity

$$\begin{aligned} \bar{\rho}_j^{n+1} &= \rho_j^n + \frac{1}{8}\frac{r_{j-1/2}}{r_j}(\rho_{j-1}^n - \rho_j^n) + \frac{1}{8}\frac{r_{j+1/2}}{r_j}(\rho_{j+1}^n - \rho_j^n) \qquad (2.16)\\ &= \rho_j^n + \frac{1}{8}(\rho_{j+1}^n - 2\rho_j^n + \rho_{j-1}^n) - \frac{1}{2}\frac{1}{8}\frac{\Delta r}{r}(\rho_{j-1}^n - \rho_j^n) + \frac{1}{2}\frac{1}{8}\frac{\Delta r}{r}(\rho_{j+1}^n - \rho_j^n). \end{aligned}$$

The difference due to geometry lies in the last two terms of eq. (2.16). To maintain the conservation of the transported quantity, the flux limiter has to be modified in such a way that when the diffusion is not removed, a part corresponding to these two terms is also added. Also, for flux-limiting, the final result (eq. (2.6)) is not to be compared with the tentative result $\bar{\rho}_j^{n+1}$, but with a result where the geometric contribution is added, defined as

$$\hat{\rho}_{i,j}^{n+1} = \bar{\rho}_j^{n+1} - \frac{1}{r}\rho_j v_j^2 \Delta t \tag{2.17}$$

for baryon density and analogously for other densities. This result is used only for defining the need for flux correction and the antidiffusive flux itself is defined as in eq. (2.8). Now the corrected antidiffusive fluxes can be written as

$$A_{j+1/2}^c = C_{j+1/2}A_{j+1/2} - \frac{1}{2}(\frac{1}{8} - C_{j+1/2}\eta)\frac{\Delta r}{r}(\bar{\rho}_{j+1}^{n+1} - \bar{\rho}_j^{n+1}), \tag{2.18}$$

where the factor $1/8 - C_{j+1/2}\eta$ is close to zero when there is no need for flux correction ($C_{j+1/2} = 1$) and diffusion is removed. On the other hand, when diffusion is large ($C_{j+1/2} \approx 0$) and might break the conservation laws, additional terms required by eq. (2.16) are added.

These both approaches give similar results within a few percent accuracy. The first one is somewhat more transparent whereas the latter is more flexible and can be modified for other non-cartesian coordinates as well.

2.2 Equation of State

The actual equation of state (EoS) of strongly interacting matter at high temperatures and densities is still largely unknown. At temperatures well below the pion mass the equation of state for a dilute hadron gas can be calculated reliably by using a virial expansion with input from empirical scattering cross sections [13]. However, at temperatures larger than pion mass, third and higher order virial coefficients become important and at present there is no reliable way to compute them. On the other hand, at low temperatures a gas of free hadrons and resonances has been found to approximate an interacting hadron gas reasonably well [13]. Therefore, when an EoS for hadron gas is needed, it is often approximated by an EoS of free resonance gas even at high temperatures [I,14,15].

Generalisation of the resonance gas to the non-zero chemical potential is simple but at low temperatures and high baryon densities the repulsive interactions between particles have to be taken into account. Otherwise the hadron phase is preferred over the plasma phase. The effect of repulsive interactions can be included either by adding an excluded volume correction [15] or a repulsive mean field potential coupling to the net baryon density [I].

The hadronic equation of state is also affected by the in-medium modifications to effective particle and resonance masses. In principle these are straightforward to take into account in a free resonance gas model, but it would require exact knowledge of the temperature and density dependence of effective masses. So far this knowledge has not been obtained and it is even uncertain whether hadrons gain or lose mass in hot and dense matter [14]. Thus any equation of state containing these effects is highly model dependent.

The equation of state of quark-gluon plasma is not easily calculable either. Even if QCD is an asymptotically free theory, perturbative methods are not applicable at temperatures close to T_c which are attainable in heavy ion collisions. Thus the only rigorous method of computing the EoS of strongly interacting matter is a numerical simulation of QCD on lattice. For pure SU(3) theory where no quarks exists the calculations give a phase transition temperature of $T_c = 265^{+10}_{-5}$ MeV [16]. Unfortunately the extrapolation to continuum limit is not as well understood when quarks are included in the simulations. Therefore the precision of the results is worse and the simulations give only an estimate of the phase transition temperature to be $T_c \lesssim 170$ MeV or $T_c \approx 150$ MeV depending on the method used for converting the results to the physical units [2].

At the moment the question of the order of the phase transition is equally unclear. So far the result depends on the number of quark flavours and quark masses used in the simulations. For pure glue and QCD with four massless quarks, lattice results indicate a first order phase transition whereas for two or three massless quarks the phase transition is most probably of second order [17]. For the most realistic scenario with two light, although not massless, and one heavy quark the order of the phase transition seems to depend on the numerical values of the quark masses. It is even possible that the transition might be

	EoS A	EoS B	EoS D	EoS H
K (fm^3 MeV)	450	660	450	450
$B^{1/4}$ (MeV)	235	200	264	–
T_c at $\mu = 0$ (MeV)	165	140	200	∞

Table 2.1: Parameter values characterising different equations of state. Notice that even if EoSs A and H have different number of hadronic degrees of freedom in papers I–III and paper IV, these parameters are the same in both cases. For details, see the text.

smeared to a rapid crossover instead of a sharp transition [18]. One has to also bear in mind that all lattice results quoted above are obtained for $\mu_b = 0$. There have been attempts to make lattice calculations at finite chemical potentials too, but so far the only result with physical meaning available from these calculations is the existence of a finite density phase transition at a critical value of baryon chemical potential, μ_c [2].

In the studies of this thesis the equations of state have been constructed using a resonance gas approach with a repulsive mean field potential for the hadronic part and a bag model EoS of an ideal massless parton gas for the plasma part. These parts are joined using the Maxwell construction. In the hadron phase the strength of the repulsive interaction between baryons is determined by a mean field repulsion parameter K. The effective baryon chemical potential is thus $\mu_{\mathrm{B}}^{\mathrm{eff}} = \mu_{\mathrm{B}} - K\rho_{\mathrm{B}}$. In papers I–III the resonance gas is assumed to contain the following hadrons with their corresponding antiparticles:

$$\pi, K, \eta, \rho, \omega, K^*, p, n, \eta', \phi, \Lambda, \Sigma, \Delta, a_1, \Xi, \Sigma(1385), \tag{2.19}$$

whereas in paper IV all hadrons listed in the Particle Data Book [19] up to 2 GeV mass were used. However, the difference between EoS A of papers I–III and EoS A of paper IV is negligible. In these equations of state the temperature in the hadron phase is always below 165 MeV and the higher mass states are suppressed through the Boltzmann factor. On the other hand, the increase of the number of degrees of freedom is visible in the purely hadronic EoS H, where the larger number of included resonances leads to lower temperature and pressure at high densities. However, the energy density drops so fast during the evolution that the pressure at the very beginning affects the evolution only slightly and the differences in the evolution of the flow between the two different versions are negligible. As mentioned, plasma does not behave like an ideal gas at $T > T_c$ and $\mu_b = 0$, but there is no reliable way to extend the lattice results to non-zero baryon chemical potentials. Therefore it is more consistent to approximate QGP EoS with a bag model EoS with a number of flavours $N_f = 2.5$ to simulate effects of finite strange quark mass.

In papers I and IV a set of equations of state covering the range of phase transition temperatures indicated by the lattice calculations has been used. The

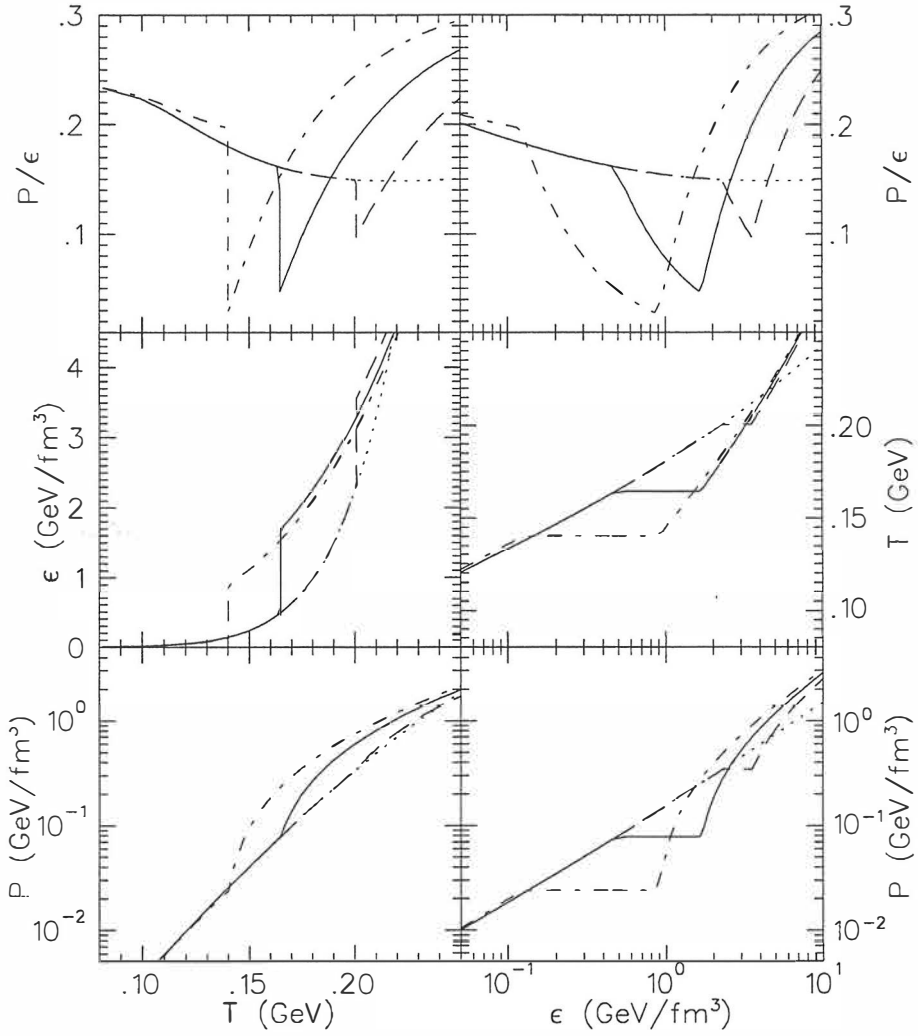

Figure 2.3: The ratio of pressure and energy density (P/ϵ), energy density (ϵ), temperature (T) and pressure (P) as functions of T and/or ϵ at baryon density $n_B = 0$ for equations of state EoS A (solid line), EoS D (dashed line) and EoS H (dotted line) from paper IV and EoS B (dash-dotted line) from paper I.

phase transition temperature depends on two parameters, the mean field repulsion parameter K and the bag constant B. The values of these parameters and the phase transition temperatures are summarised in table 2.1. The phase transition temperature $T_c = 140$ MeV of EoS B can be considered as a lower limit whereas $T_c = 200$ MeV of EoS D serves as an upper limit and $T_c = 165$ MeV of EoS A as a most probable guess. In addition to these, a purely hadronic equation of state called EoS H has been used in both paper I and IV and an

ideal gas equation of state $p(\epsilon, \rho_B) = \epsilon/3$ called EoS I in paper I. To characterise the different equations of state some of their properties are plotted in fig. 2.3. The softness of each equation of state seen in the P/ϵ ratio is also manifested in the lifetime of the fireball. The softest EoS B leads to a longer lifetime than EoS A [I] and correspondingly the lifetime is longer when EoS A is used than when EoS D is [IV].

2.3 Parametrisation of the initial state

A major problem in using hydrodynamics to describe a high energy nucleus-nucleus collision is how to combine it with the primary stage of the collision when the final state particles are produced. At low energies hydrodynamics can be used for the description of the whole collision process starting with the incoming nuclei as approaching droplets of nuclear fluid which meet, compress and heat up, followed by the expansion of this dense fireball. At high energies the nuclei become increasingly transparent and it becomes unrealistic to describe the formation of the initial dense matter in terms of hydrodynamic fusion of the colliding nuclei into a single fluid droplet. Instead, one can parametrise the formation of matter during the primary collision stage in the form of initial conditions for the subsequent hydrodynamic expansion. In principle these initial distributions should be calculated from the dynamics of strong interactions but in practice such calculations involve modelling, usually with several phenomenological parameters.

The parametrisation of recently thermalised state which can be used as an initial state of hydrodynamic evolution can be done in several ways. Two extreme scenarios are the full stopping model of Landau [6] and the boost invariant, or Bjorken model [20]. Since the former can be considered to be appropriate at moderately high energies and the latter to be an asymptotic limit when energy grows infinite, there are various parametrisations which can be used to span the range between these two extremes. Some examples of such parametrisations can be found in refs. [I,II,21,22].

In the Bjorken model the spatial energy density distribution in the global frame and at fixed time $t = t_0$ is given by [$\varepsilon_0 := \varepsilon(t_0, 0)$] [20]

$$\frac{\varepsilon(t_0, z)}{\varepsilon_0} = \left(\frac{t_0}{\sqrt{t_0^2 - z^2}} \right)^{4/3}, \tag{2.20}$$

if an ideal gas EoS, $\varepsilon = 3p$, is assumed. The central region is assumed to be baryon free in the original Bjorken model, but if one assumes the initial baryon density to be finite and boost invariant as well, the spatial baryon density distribution can be expressed as [I]

$$\frac{\rho_B(t_0, z)}{b_0} = \left(\frac{t_0}{\sqrt{t_0^2 - z^2}} \right), \tag{2.21}$$

where $b_0 := \rho_{\rm B}(t_0, 0)$. In paper I, the spatial energy and baryon density distributions are assumed to be of the forms presented above even if the initial velocity profile is not that of the Bjorken model. Instead, the velocity profile is assumed to be of the form

$$v_z(z) = \tanh(z/t_0), \qquad y(z) = z/t_0. \tag{2.22}$$

In this form t_0 should be regarded as a constant which fixes the rapidity of produced matter rather than the equilibration time.

The reason for taking the flow rapidity y, instead of velocity v_z, to be proportional to z is entirely practical. For numerical calculations, initial conditions have to be smoothed and extended over the edge of produced matter, initially at z_0. The above parametrisation leads to the Bjorken limit in the inner part ($z/t_0 \ll 1$) and extrapolates the velocity to unity smoothly in the outer parts, where the densities approach zero.

In the same way the density distributions have to be cut off smoothly at the boundaries of the phase space. In this parametrisation smoothing is done by multiplying the distributions with a Fermi function

$$f(x, x_0, a_x) = \frac{1}{\exp[(|x| - x_0)/a_x] + 1}, \tag{2.23}$$

where x_0 is the size and a_x the diffuseness parameter. Also the finite transverse size of the nuclei has to be taken into account. This is done by multiplying the distributions with another Fermi function and the initial distributions are given by equations

$$\begin{aligned} \varepsilon(z, r) &= \varepsilon_0 \left(\sqrt{1 - (z/t_0)^2}\right)^{-4/3} f(z, z_0, a_z) f(r, r_0, a_r), \\ \rho_B(z, r) &= b_0 \left(\sqrt{1 - (z/t_0)^2}\right)^{-1} f(z, z_0, a_z) f(r, r_0, a_r). \end{aligned} \tag{2.24}$$

This kind of a parametrisation is simple and easy to understand but it has one unattractive feature. It assumes the nuclei to be almost transparent. At the SPS energies, it is an acceptable approximation for sulphur size nuclei but in lead on lead collisions this assumption is improbable. Also, the parametrisations of this kind do not provide any way of comparing collisions of different nuclei since the parameter values and in some case the entire parametrisation have to be chosen for each collision separately.

The parametrisation presented in papers II and III tries to avoid these drawbacks by parametrising the initial baryon stopping locally in the transverse direction in terms of the nuclear thickness function and constraining the energy density from conservation of energy. The starting point is the parametrisation of the rapidity distribution of baryons as a sum of contributions from the target and projectile nucleus,

$$\begin{aligned} \frac{dN_{\rm B}}{dy} &= \frac{dN_{\rm B}^{\rm P}}{dy}(x_y) + \frac{dN_{\rm B}^{\rm T}}{dy}(x_y) \\ &= \left[C^{\rm P} \exp(a x_y^3 + b x_y^2 + c x_y) + C^{\rm T} \exp(-a x_y^3 + b x_y^2 - c x_y)\right] (1 - x_y^2)\, \theta(1 - x_y^2), \end{aligned} \tag{2.25}$$

using a variable $x_y = y/y_{\max}$, the rapidity scaled with $y_{\max} = y^{\mathrm{P}}_{\mathrm{cm}}$, the projectile rapidity in the cm frame. The factor $(1 - x_y^2)$ ensures that the distribution goes to zero at the boundary of the phase space when effects like Fermi motion are neglected. C^{P} and C^{T} are normalisation constants. The functional form is motivated by the experimental proton rapidity distributions in $p + p$ collisions [II] and the possibility to control the amount of stopping. The main idea of this parametrisation is that the amount of stopping is determined locally in transverse plane: the baryon distribution, e.g. at distance $r = 1$ fm from the collision axis, is *different* from the distribution at $r = 2$ fm. This is implemented by defining the parameters $a(T_A)$, $b(T_A)$ and $c(T_A)$ as functions of the local nuclear thickness

$$T_A(r) = \int dz\, n_{\mathrm{B}}(z, r)\,, \tag{2.26}$$

where $n_{\mathrm{B}}(z, r)$ is the nuclear density for a nucleus of mass number A, z is the longitudinal and r the transverse coordinate. Due to the assumed cylindrical symmetry, the impact parameter $b = 0$ and the transverse coordinate r is the distance from the beam axis for both the target and projectile nuclei. In this thesis the nuclear density is given by the Woods-Saxon parametrisation

$$n_{\mathrm{B}}(z, r) = \frac{n_0}{\exp[(\sqrt{z^2 + r^2} - R_A)/a_R] + 1}\,, \tag{2.27}$$

with

$$R_A = 1.12\ \mathrm{fm} \times A^{1/3} - 0.86\ \mathrm{fm} \times A^{-1/3}\,, \tag{2.28}$$

$a_R = 0.54$ fm and $n_0 = 0.17\ \mathrm{fm}^{-3}$ [23]. The functional dependence of a, b and c on T_A is chosen to be

$$\begin{aligned} a(T_A) &= 1.5\,(\sigma_{pp}\, T_A)^{-1} \\ b(T_A) &= \beta_s\,(1 - \sigma_{pp}\, T_A) \\ c(T_A) &= 3.0\,, \end{aligned} \tag{2.29}$$

where $\sigma_{pp} = 32$ mb is the total inelastic cross section for p+p collisions at the SPS energy. This choice of fixing the dependence of parameters a, b and c on nuclear thickness is relatively simple and in the case of one collision, i.e. $\sigma_{pp}\, T_A = 1$, the experimental proton rapidity distribution for $p + p$ collisions is recovered [II]. For $\sigma_{pp}\, T_A > 1$, the b coefficient is negative indicating increasing stopping with growing nuclear thickness, the strength being controlled by β_s. It is fixed from fits to baryon rapidity spectra in heavy ion collisions and therefore its determination includes the hydrodynamical evolution. Changing the hydrodynamical evolution by choosing different initial energy and (longitudinal) velocity distributions or equation of state results in a different optimal value for β_s (see table 2.2).

The rapidity distribution of energy density is assumed to be gaussian:

$$\frac{dE(r)}{dy} = C_\varepsilon \exp\left[\frac{-(y - y_0)^2}{2\sigma_\varepsilon^2}\right]\left[1 - (y/y_{\max})^2\right]\theta(1 - (y/y_{\max})^2)\,, \tag{2.30}$$

where the width σ_ε and the normalisation C_ε depend on the transverse coordinate r. The value y_0 is identified with the center-of-mass rapidity of the collision locally in the transverse plane. Since our hydrodynamic calculation is performed in the overall center-of-mass frame of participating nucleons, $y_0(r) \equiv 0$ for zero impact parameter collisions of equal nuclei. For asymmetric collisions the thickness of target and projectile varies differently with transverse radius r and therefore the rapidity of the local cm frame $y_0(r)$ changes in the transverse plane.

It turns out that the experimental pion rapidity distribution is well reproduced when the value of the width σ_ε correlates with the baryon stopping. A larger stopping of baryon number results in a larger stopping of energy, too. Therefore the width of the energy distribution in rapidity space decreases with increasing nuclear stopping. This is described with an ansatz

$$\sigma_\varepsilon(r) = \frac{c_\varepsilon}{[\sigma_{pp} T_A(r) \sigma_{pp} T_B(r)]^{\alpha_\varepsilon}}, \tag{2.31}$$

where σ_{pp} is included to make the denominator dimensionless. The constants c_ε and α_ε are determined from an overall fit to the investigated collision systems (see table 2.2).

The normalisation constants, C^P and C^T for baryon and C_ε for energy density, are given by local baryon number and energy conservation. The baryon number and energy per unit transverse area at r are required to be the same in the fireball than in the colliding nuclei. However, in a nucleus-nucleus collision a certain fraction of nucleons never suffer a single collision. These nucleons are not detected in the experiment and their energy does not contribute to the production of final matter. To account for this, the normalisation constants are scaled so that the baryon number and energy of the fireball are a certain fraction $\xi \lesssim 1$ of the baryon number and energy of the colliding nuclei.

So far the density distributions are specified only as functions of velocities. This leaves the freedom to change spatial distributions by changing the initial velocity profile. In papers II and III the velocity profile is of the same kind than in paper I: the initial flow rapidity is assumed to increase linearly as a function of the longitudinal coordinate z (see eq. (2.22)). However, the profile differs in such a way that the proportionality constant $1/t_0$ has now a slight dependence on the transverse radius r (see paper II). The values of $t_0(r = 0)$ are called τ_0^{eff} and presented in table 2.2.

This kind of a velocity profile leads to a spatial energy distribution which is strongly peaked in the middle of the fireball. By changing the profile, energy and baryon number can be distributed more evenly. In paper IV two different velocity profiles were used to distribute energy and baryon number in different ways and the dependence of electromagnetic spectra on these distributions was studied. The first profile, called IS 1, was similar to the one used in papers II and III. The second, IS 2, was made by subtracting an additional function of z from the original velocity parametrisation (eq. (2.22)) and changing the value of τ_0^{eff} parameter slightly. The resulting profile has a flatter velocity gradient in the middle of the fireball and a steeper gradient close to the edge than the original

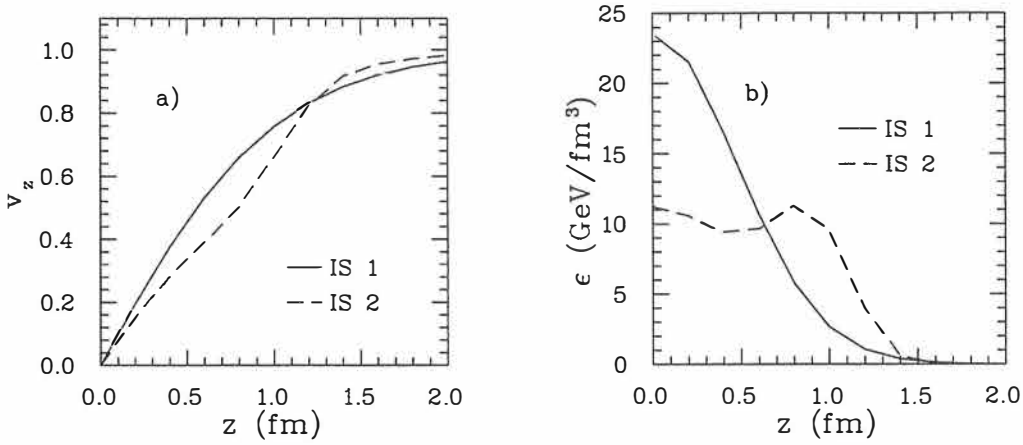

Figure 2.4: Initial velocity profile (a) and energy density profile (b) for EoS D used in paper IV.

	Paper II		Paper III				
collision	S + S	Pb+Pb	S + S	O + Au	S + Ag	S + Au	Pb + Pb
ξ	0.9	0.9	0.9	1.0	0.9	0.95	0.9
$\tau_0^{\rm eff}$	1.2	1.3	1.2	1.4	1.4	1.5	1.3
β_s	2.25	2.25	2.25	2.25	2.25	2.25	2.25
c_ϵ	0.75	0.75	0.8	0.8	0.8	0.8	0.8
α_ϵ	0.13	0.13	0.125	0.125	0.125	0.125	0.125

	Pb + Pb in paper IV					
	IS 1			IS 2		
EoS	A	D	H	A	D	H
ξ	0.98	1.0	1.0	0.9	0.9	0.9
$\tau_0^{\rm eff}$	1.0	1.0	1.0	0.84	0.84	0.84
β_s	2.25	2.0	2.0	1.5	1.5	1.5
c_ϵ	0.75	0.75	0.75	1.2	1.2	1.2
α_ϵ	0.125	0.125	0.125	0.125	0.125	0.125

Table 2.2: Summary of parameter values used for different collisions, equations of state and initial states in papers II–IV.

profile IS 1. These velocity profiles and consequent energy density distributions are illustrated in fig. 2.4. It is important to notice that to reproduce the data, IS 2 requires less stopping than IS 1. Therefore the parameter values defining the rapidity distributions (eqs. (2.25) and (2.30)) are slightly different in these two cases (see table 2.2).

The actual values of the parameters used in the papers reviewed here are collected in table 2.2. Even if the goal was to create one parametrisation for

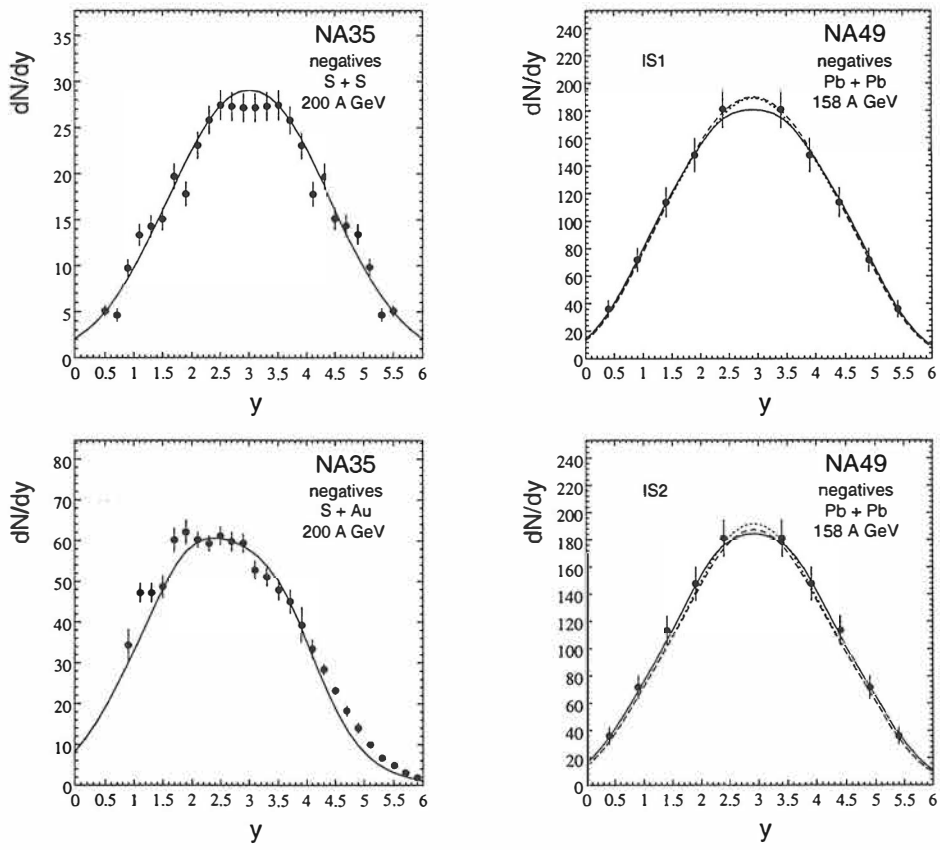

Figure 2.5: Rapidity distributions of negative particles in various collisions. The equation of state is EoS A (solid line), EoS D (dotted line) or EoS H (dashed line). IS 1 and IS 2 refer to different initial states (see text). The data are S+S [24], S+Au [25] and Pb+Pb [26]. The Pb+Pb data are preliminary.

all collisions at the SPS energy, the parameter values vary slightly from paper to paper. This is partly due to the evolution of the model and partly due to different scopes of each paper. In paper II the model was in an early stage of its development and it was used for two symmetric collisions only whereas in paper III it was refined to span all the nucleus-nucleus collisions measured at the CERN SPS. On the other hand, in paper IV, the goal was to study one collision using different equations of state and search the extremes in the initial energy distributions still reproducing the measured hadron spectra. Therefore, even if the linear z-dependence of velocity profile IS 1 in paper IV is similar to the velocity profile used in paper III, the values of τ_0^{eff} parameter differ resulting in a larger initial energy density in the calculations of paper IV than of paper III.

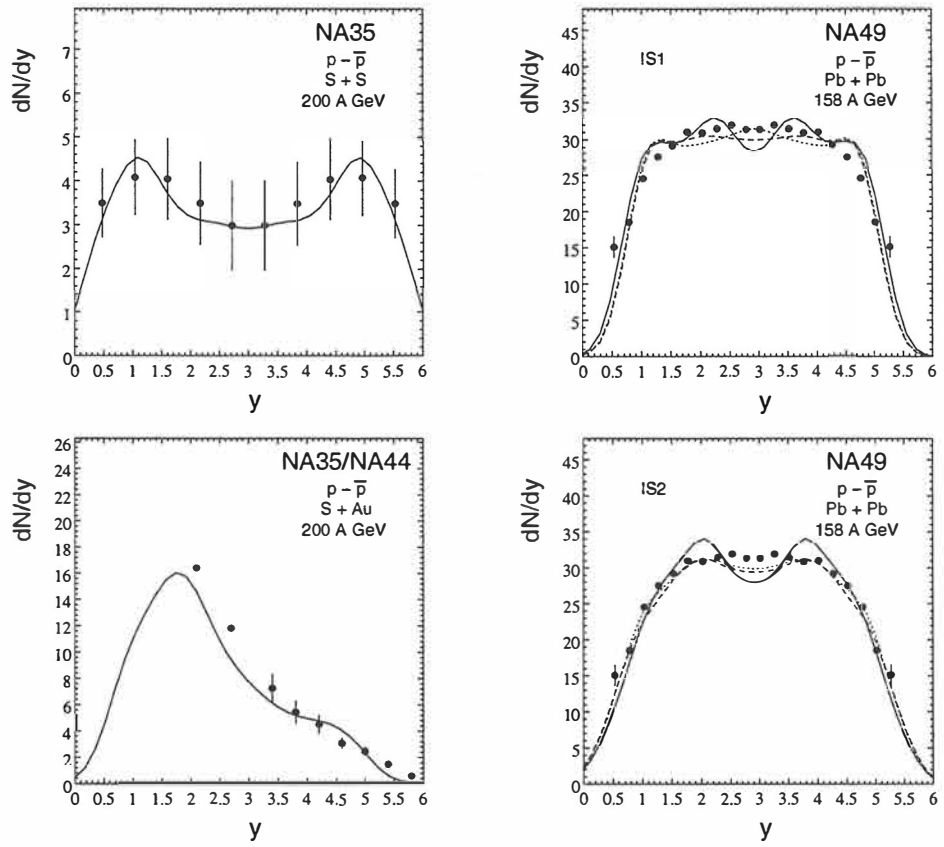

Figure 2.6: Rapidity distributions of $p - \bar{p}$ in various collisions. The equation of state is EoS A (solid line), EoS D (dotted line) or EoS H (dashed line). IS 1 and IS 2 refer to different initial states (see text). The data are S+S [24], S+Au ($y > 3$ data from NA35 [27] and two data points with $y < 3$ are proton data from NA44 [28]) and Pb+Pb [29]. The Pb+Pb data are preliminary.

The final justification for the parametrisation presented here comes from its ability to reproduce the observed data[3]. In paper III results for five different A+B collisions at SPS energies are presented. As a summary results for S+S and S+Au collisions for EoS A [III] and for Pb+Pb collision for three different EoSs and two different initial velocity profiles [IV] are shown here.

The rapidity distributions of negative particles (fig. 2.5) are well reproduced in all the cases. This suggests that the parametrisation might be applicable for any colliding nuclei at the SPS energies. Also the different velocity profiles used to model Pb+Pb collision produce equivalent results, which tells that de-

[3]Calculation of hadron spectra is described in section 2.4.

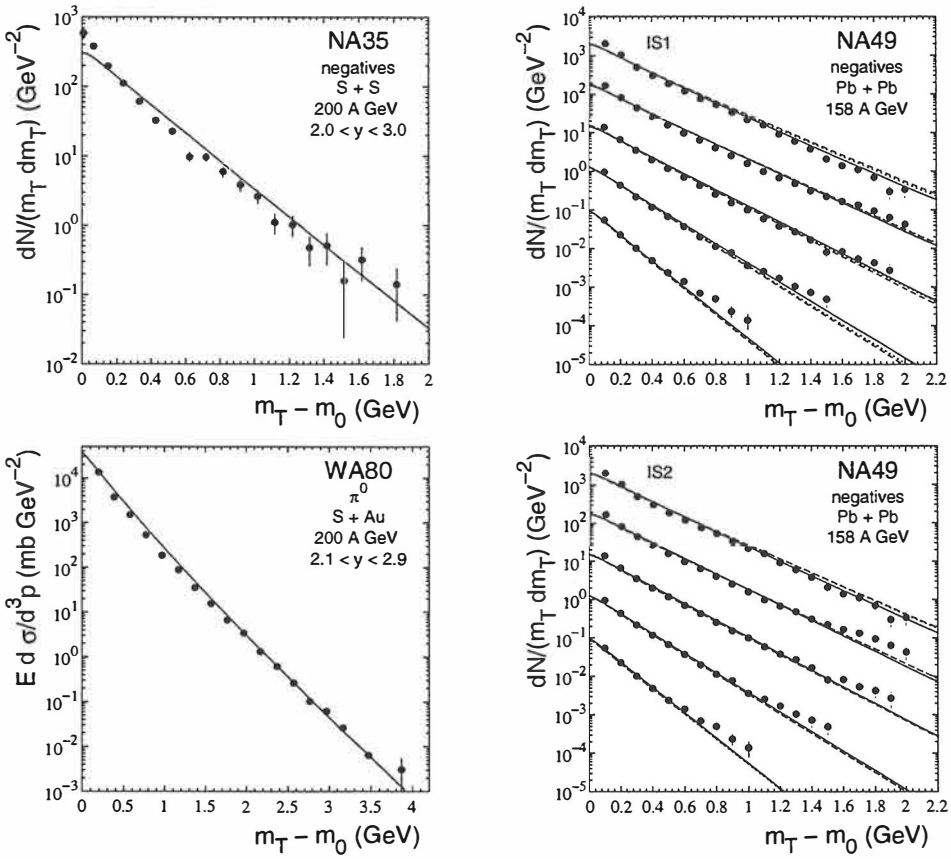

Figure 2.7: Transverse momentum distributions of negative particles and π^0 in various collisions. The equation of state is EoS A (solid line), EoS D (dotted line) or EoS H (dashed line). IS 1 and IS 2 refer to different initial states (see text). The data are S+S [24], S+Au [30] and Pb+Pb [26] for rapidity intervals of width 0.5 and center at (top to bottom) 3.4, 3.9, 4.4, 4.9, 5.4. These data sets are successively scaled down by 10^{-n},$n = 0, 1, 2, 3, 4$. The Pb+Pb data are preliminary.

spite shifting thermal energy to kinetic energy, the final energy flow through freeze-out surface is roughly similar in both cases However, the hydrodynamical evolution does not smooth away all the differences of the initial conditions since the net proton rapidity spectra differs slightly (fig. 2.6). The parameter values are not fine-tuned to reproduce the net proton spectra of Pb+Pb collision since the available data were preliminary when these simulations were carried out. In

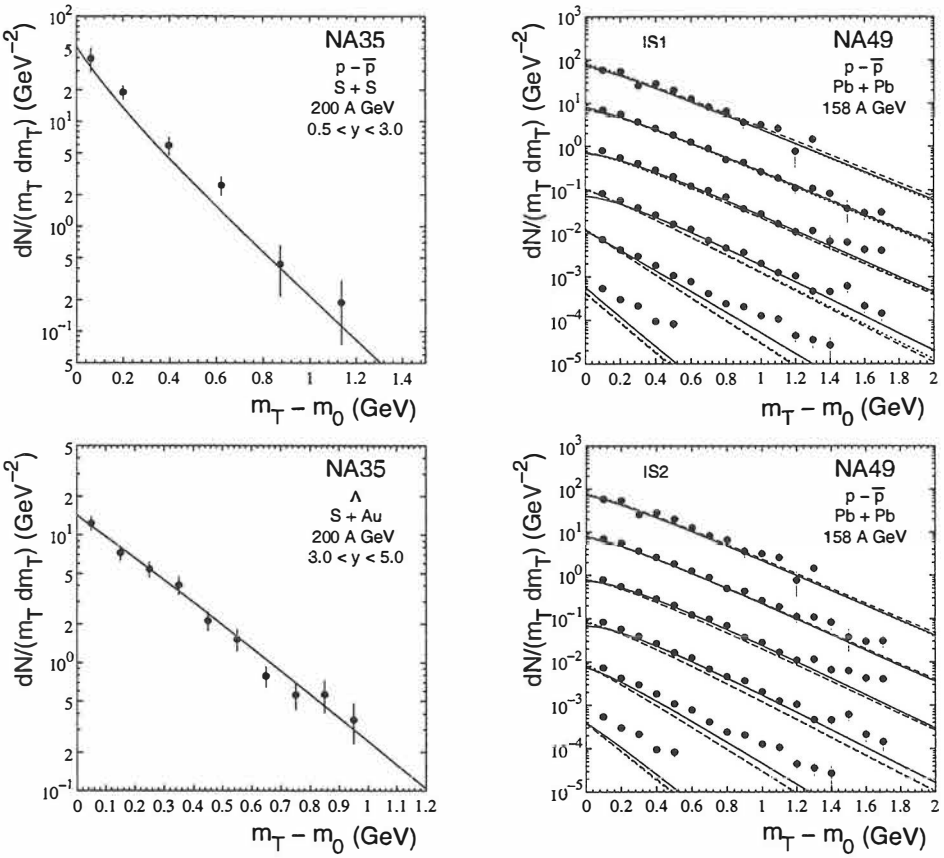

Figure 2.8: Transverse momentum distributions of $p - \bar{p}$ and Λ in various collisions. The equation of state is EoS A (solid line), EoS D (dotted line) or EoS H (dashed line). IS 1 and IS 2 refer to different initial states (see text). The data are S+S [24], S+Au [31] and Pb+Pb [26] for rapidity intervals of width 0.5 and center at (top to bottom) 2.9, 3.4, 3.9, 4.4, 4.9, 5.4. These data sets are successively scaled down by 10^{-n},$n = 0, 1, 2, 3, 4, 5$. The Pb+Pb data are preliminary.

retrospect this was a right choice since the data has changed noticeably[4]. The net proton rapidity spectra of S+S collision demonstrates smaller baryon stopping in smaller nuclei, which the parametrisation is able to reproduce. Also the distribution in S+Au collision is concentrated at the target fragmentation region as expected.

The general features of the transverse momentum distributions presented in figs. 2.7 and 2.8 are well reproduced too. The main discrepancies are at

[4]See the most recent data in [32].

the spectra of high rapidity net protons of Pb+Pb collisions. In a nucleus-nucleus collision there are always a few protons suffering no more than a single collision. Therefore these protons are not thermalised and hydrodynamics cannot reproduce their behaviour. The slightly concave shape of most p_T spectra is not reproduced either. This is most probably due to the too simple freeze-out procedure applied in the calculation (see the discussion about freeze-out in section 2.4).

The model can reproduce the spectra of Λ's in S+Au collisions (fig. 2.8 and paper III) but not in Pb+Pb collisions (see paper IV). It also fails to reproduce kaon spectra in both cases. The failure is almost easier to understand than the success. The spectra are calculated assuming full chemical equilibration until the thermal freeze-out, but more detailed thermal models indicate that the particle ratios are fixed already at higher temperature (chemical freeze-out) than the thermal freeze-out temperature and that the strange particles are not in chemical equilibrium but their abundancies are suppressed [33]. The strangeness suppression and higher chemical freeze-out temperature lead to a situation where the equilibrium abundancies of some of the strange particles at thermal freeze-out temperature may accidentally coincide with the experimental ones like the yield of Λ's in S+Au collisions. Another similar coincidence is the ϕ/h^- ratio in Pb+Pb collisions, which is not reproduced at thermal freeze-out temperature $T_f \approx 140$ MeV, but is reproduced at $T_f \approx 120$ MeV. The ϕ yield is important for the background to thermal low mass electron pairs and is discussed in section 3.3.1.

The failure to reproduce the strange particle yields does not invalidate the space-time evolution the model describes, since the evolution and properties of the fireball are governed by the most copious particles of the fireball, i.e. pions and nucleons, which spectra are reproduced. Thus, for calculating the thermal electromagnetic emission, the mismatch in the yields of strange particles does not constitute a serious error.

As one may expect, the lower initial energy density of IS 2 leads to somewhat weaker flow than IS 1, but the differences are small and both initial configurations lead to acceptable description of the data (see also section 2.4). However, even if these two very different initial states reproduce the observed hadron spectra, it has to be stressed that any initial state does not. To achieve acceptable results the initial velocity distribution can be chosen relatively freely, but after fixing the velocity distribution, the density distributions have to be very carefully fine-tuned or vice versa. The conclusion of this exercise is not that anything goes but that even if the space of allowed parameter values is not a single point, it is a small subset of the entire parameter space.

2.4 Treatment of freeze-out

Since the thermodynamical variables of hydrodynamical description are not experimentally observable there has to be a transition from particle fluid to free-

streaming particles in the model. This so-called freeze-out is not a result of hydrodynamics but has to be modelled separately. In principle the choice is obvious: the particles cease to interact and start to behave as free-streaming ones when the mean free path of particles (λ) is no longer small compared to the size of the system (R). Since $\lambda \propto (n\sigma)^{-1}$, the mean free path can be correlated with the density of the system and a dilute enough part of the system can be considered as non-interacting i.e. frozen out. However, for a consistent treatment one has to solve hydrodynamical equations in a spacetime region where the mean free path is small enough, kinetic equations outside this region, search for the boundary between these two regions using the criterion described above and match the densities on this boundary. Such an approach is quite complicated and tedious and has not been carried out rigorously [7].

In practice the problem of finding the boundary between kinetic and hydrodynamical descriptions is usually – and also in this thesis – circumvented by assuming that the hydrodynamical description is valid to arbitrarily low densities. In this way one may solve the continuity equations in the entire space-time region and choose the freeze-out surface to be a surface of constant temperature or energy density *afterwards,* when the evolution of the fluid is known.

The assumption of the freeze-out surface to be a surface of constant temperature is based on the argument that since $n \propto T^3$, for constant cross section σ the mean free path is proportional to T^{-3}. Therefore, after the temperature falls below a certain limit, the mean free path is longer than the system size and the particles decouple. The mean free path is different for different particles and therefore particles should freeze out at different temperatures. However, freeze-out at different temperatures as advocated in [34] leads to a situation where in the same fluid cell there are both decoupled, free-streaming particles and interacting particles in kinetic equilibrium. It is very difficult to specify the appropriate equation of state to be used in such a region. In this thesis this difficulty is avoided in the most obvious way by choosing all particle species to freeze out at the same temperature.

The inelastic scatterings which change particle species have lower cross sections than the elastic ones and therefore one may argue that the chemical composition of the final stage is fixed (chemical freeze-out) in a higher temperature than the particle distribution in the phase space (thermal or kinetic freeze-out). The concept of separate chemical and thermal freeze-out temperatures is supported by thermal model calculations where the relations of particle abundancies can be reproduced assuming $T = 170$–190 MeV temperature [33,35,36] whereas the values of the thermal freeze-out temperature fitting the data are lower (see below). In the hydrodynamical model of this thesis, the chemical equilibrium is, however, assumed to be maintained during the entire evolution, i.e. the chemical and thermal freeze-out temperatures are the same. In principle it is possible to construct a hydrodynamical model where the chemical freeze-out takes place before the thermal freeze-out, but this requires a separate chemical potential for each hadron species. If the number of hadronic degrees of freedom is large, the

corresponding equation of state would be very complicated and therefore this approach has not been carried out. Also the thermal models assume a homogeneous fireball in a global thermal equilibrium whereas the hydrodynamical models assume a local thermal and chemical equilibrium. Due to this discrepancy the comparison of the results of these models is not straightforward.

The choice of a freeze-out at a surface of constant temperature implies another simplifying assumption namely that the "thickness" of the freeze-out surface is infinitesimal. In practice there is – due to the finite size of the system – a finite probability for a single particle to escape without rescattering even from the densest part of the fireball, but approaches where this has been taken into account [37] are difficult to implement technically.

By making all the assumptions described above one may calculate single inclusive spectra of particles in a rather straightforward way using the Cooper-Frye formula [38] where the invariant momentum distribution of a hadron h is given by

$$E\frac{dN}{d^3p} = \frac{g_h}{(2\pi)^3}\int_{\sigma_f}\frac{1}{exp[(p_\mu u^\mu - \mu)/T] \pm 1}p^\mu d\sigma_\mu, \tag{2.32}$$

where the temperature $T(x)$, chemical potential $\mu(x)$ and flow velocity $u^\mu(x)$ are the corresponding values on decoupling surface σ_f. Besides its relative simplicity, this approach has the advantage that both energy and momentum are conserved without any extra considerations. However, the Cooper-Frye formula has a conceptual problem. At those areas where the freeze-out surface is spacelike, the product $p^\mu d\sigma_\mu$ may be either positive or negative, depending on the value and direction of p^μ. In other words, the number of particles freezing out at some part of the freeze-out surface may be negative. The problem is not quite as bad as it first looks. First, the fireball is not expanding to a complete vacuum. There are particles outside it, even if they cannot be assumed to obey thermal distribution. Second, these negative contributions are necessary to maintain energy and momentum conservation. What goes inside the surface as negative contribution comes later out and is added onto spectra. These negative contributions do not completely invalidate the prescription of Cooper and Frye, but due to them one can not specify the particle emission at different parts of the surface, which would be necessary to study the particle emission as a function of time or as a function of source size. They are also a good reminder that the whole procedure is approximative and the results obtained using it have to be taken as they are – as approximations.

There have been some attempts to solve this conceptual problem by modifying the thermal distribution used in the Cooper-Frye formula [39,40]. However, to conserve energy, these approaches necessitate the use of different value of flow velocity inside and outside the freeze-out surface. If one treats the freeze-out surface as a conventional hydrodynamical discontinuity there is nothing suspicious in this, but as mentioned, it is unlikely that the freeze-out really takes place on a thin surface. Thus the treatment of the freeze-out as a discontinuity strengthens the approximation of a thin surface and a removal of one approximation ends up

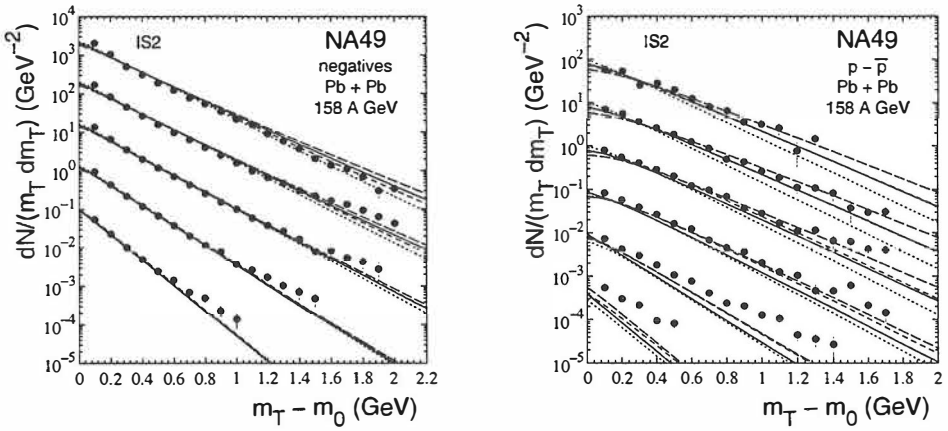

Figure 2.9: Transverse momentum distributions of negative particles and $p - \bar{p}$ in Pb+Pb collision for different EoSs and freeze-out temperatures. Solid line is EoS D with $T_f \approx 140$ MeV, long dashed line EoS D with $T_f \approx 120$ MeV, dotted line EoS A with $T_f \approx 140$ MeV and short dashed line EoS A with $T_f \approx 120$ MeV. Initial state is IS2. Data are from the NA49 collaboration [26] and presented like in figs. 2.7 and 2.8.

making another approximation even more important.

In this thesis, the freeze-out has been realised using the conventional Cooper-Frye procedure for each hadron included in the EoS. The contributions from unstable resonances are then added to the stable hadron spectra using the approximations and decay kinematics described in ref. [41]. Finally, the results are integrated over the experimental acceptance in p_T and y.

The calculations comparing the various mean free paths of the hadrons in the fireball with its size suggest the freeze-out temperature to be about 140 MeV [42]. The S+Au collision data can be fitted using this freeze-out temperature [I,III], but recently there have been studies where freeze-out temperature of 120 MeV has been found to be more appropriate to describe Pb+Pb collision data [43–45]. On the other hand the data has been successfully fitted using approximately 140 MeV freeze-out temperature as well [46,IV].

The effect of the freeze-out temperature on transverse momentum spectra calculated using the hydrodynamic approach presented here can be seen in fig. 2.9 where p_T spectra of negative particles and net protons is presented. The spectra are calculated using decoupling energy densities $\epsilon_f = 0.14$ GeV/fm^3 ($T_f \approx 140$ MeV) and $\epsilon_f = 0.069$ GeV/fm^3 ($T_f \approx 120$ MeV). For comparison the results presented here are obtained using initial state IS2, not IS1 like in paper IV. As expected, the lower initial pressure leads to a weaker flow than in the case of IS1 and therefore the slopes of the spectra are steeper than those presented in

paper IV. This makes the favoured combinations of EoS and decoupling temperature less clear. However, the overall behaviour is similar; negative particles consist mostly of light pions and for them the larger flow produced by the later freeze-out is compensated by a lower temperature and all these combinations of EoS and freeze-out temperature produce almost identical spectra. On the other hand, heavier protons gain more with an increased flow velocity than they lose with a decreased temperature and the later freeze-out produces flatter spectra.

The stiffness of the equation of state affects flow velocity too. Around midrapidity ($y = 2.9, 3.4, 3.9$) the spectra obtained using either EoS A and $T_f \approx 120$ MeV or EoS D and $T_f \approx 140$ MeV are almost identical. At larger rapidities the situation is different and the results obtained using the same freeze-out temperature but different equations of state are close to each other. The explanation for this behaviour is easy: high rapidity protons originate mostly from those regions where initial longitudinal velocity has been large. In these regions initial temperature has also been very close to the phase transition temperature which means that the effective part of the equation of state is almost similar in both cases and the effect of the freeze-out temperature on flow dominates. Thus the combination of EoS A and $T_f \approx 120$ MeV produces the best fit to the data but the difference to the fits obtained using EoS D and $T_f \approx 140$ MeV is visible only at large rapidity net protons. It is doubtful how well these protons are thermalised and whether their spectra are describable using hydrodynamical model at all. Therefore one can say that both of these combinations produce acceptable fit to the data whereas the other combinations of EoS and T_f produce too large or small flow.

Since the idea of this thesis has been to choose the parameters of the model to reproduce the hadron data, the freeze-out temperature used in the calculations has been $T_f \approx 120$ MeV for EoS A in Pb+Pb collision and $T_f \approx 140$ MeV for EoS D unless otherwise mentioned. When EoS H is used, the spectra depend on the freeze-out temperature in the same way than when EoS D is used. Therefore EoS H is also combined with $T_f \approx 140$ MeV. In S+Au collisions the freeze-out temperature is always $T_f \approx 140$ MeV.

The hydrodynamical model fits the data at various values of freeze-out temperature assuming that the equation of state is chosen accordingly, whereas other approaches fix the temperature. One of the differences leading to different results is that in [43] the freeze-out takes place at constant temperature but in this thesis at constant energy density. The latter approach leads baryon rich areas to decouple at lower temperatures than baryon poor areas.

However, the main reason for different freeze-out temperatures lies in the different velocity profiles of these approaches – the p_T-spectra do not depend only on $\langle v_T \rangle$ and T but on flow pattern as well (the importance of velocity profile has also been stressed in ref. [47]). In refs. [43,44] the velocity profile is linear and in ref. [45] radial velocity is assumed to be constant whereas a realistic hydrodynamical evolution used in refs. [46,IV] gives much more complicated flow pattern. Therefore the ambiguity between freeze-out temperature and radial flow

velocity cannot be solved using single particle spectra alone but more information is needed. HBT analysis is one way to reduce this ambiguity.

When comparing different approaches to determine the freeze-out temperature it is also useful to remember that all the approaches assume that the freeze-out temperature of all the hadron species is the same. In refs. [43–45] this is a necessary requirement to reduce the ambiguity between T_f and $\langle v_T \rangle$. As discussed earlier, in the hydrodynamical models all the species freeze out in the same temperature for practical reasons. Since the cross sections are not the same for all particle species, the freeze-out temperatures may differ too. On the other hand, as shown here, it is possible to fit the data assuming the same freeze-out temperature for protons and pions. Thus it is probable that the difference in the freeze-out temperature of these particles is not large.

Chapter 3

Thermal electromagnetic emission

In the context of heavy-ion collisions thermal emission does not mean that the emitted photons and leptons would have the customary spectrum of black-body radiation, which depends only on the temperature of the system. The spectrum deviates from the thermal one since the mean free path of photons and lepton pairs is much longer than the size of the system. The produced photons and lepton pairs do not rescatter after being formed and therefore do not reach thermal equilibrium with the ambient matter. Thus the spectrum of photons and lepton pairs reflects the dynamics of the production reactions in the matter, which may be different in different phases. Similarly, due to the long mean free path, the photons and dileptons produced at all stages of the collision can be observed and their spectra reflect the properties (i.e. temperature, evolution of flow, etc.) of the fireball in a more direct way than the hadron spectra. The observed spectra is a convolution of emission at different temperatures and (possibly) phases which makes it difficult to get a clear signal of a phase transition or to specify the evolution leading to a particular spectrum. However, as will be shown in the following sections, the comparison of various spectra can still give useful information about the evolution.

In the QGP the photon production is dominated by the QCD Compton and annihilation reactions, $qg \to q\gamma$, $\bar{q}g \to \bar{q}\gamma$ and $q\bar{q} \to g\gamma$. The production rate due to these processes was calculated in ref. [48] and the calculation was extended to finite values of baryon density in ref. [49]. Since finite baryon density is included in the calculations of this thesis, the results of ref. [49] have been used.

The rates due to various annihilation and decay processes[1] in a hadron gas were calculated in ref. [48] and a practical parametrisations for them were given in ref. [50]. It was also shown in ref. [51] that a_1 axial vector meson contributes significantly to photon production in the π-ρ channel. Thus a parametrisation of the rate due to process $\pi\rho \to a_1 \to \pi\gamma$ given in ref. [51] is also included. These rates do not contain processes involving baryons but it has been estimated that

[1] $\pi\pi \to \rho\gamma$,$\pi\rho \to \pi\gamma$, $\omega \to \pi\gamma$ and $\rho \to \pi\pi\gamma$.

a possible contribution from baryons would be small [52].

In the plasma phase the dilepton production is dominated by the process $q\bar{q} \to l\bar{l}$. The rate due to this process was computed in lowest order for finite baryon chemical potential in ref. [53]. At low invariant masses the reactions of order $\mathcal{O}(\alpha\alpha_s)$ become also important [54]. However, the mass region where these corrections are significant is dominated by the Dalitz decays of the final mesons [55]. Therefore the higher order contributions are not taken into account in the simulations of this thesis.

The dilepton production rate in a hadron gas has recently been in the focus of large theoretical activity [56]. The in-medium properties of vector mesons are expected to differ from those of free particles [57]. Since dilepton production processes in a hadron gas involve these mesons, the changes in their properties are seen in the rates as well. However, the rates used in this thesis are calculated using the free particle properties of vector mesons. At the time of making the calculations of paper I, appropriate in-medium rates were not available and the purpose of paper IV was to study the effects of variations in initial state and phase transition temperature on electromagnetic emission. Therefore the testing of different in-medium rates within the framework of a realistic hydrodynamical model was left to a later publication [58].

In paper I the rates are those calculated by Gale and Lichard [59]. In paper IV these rates are used at masses below 1 GeV and rates by Li and Gale [60] above 1 GeV. The reason for using two different rates is that at low masses the Dalitz decays of mesons have a large contribution to the rates. Those processes were included in the rates by Gale and Lichard but not in the rates by Li and Gale. On the other hand, all the annihilation processes were given the same pion form factor in ref. [59]. This contains ρ' excitations which will add up at larger masses thus making the calculation unreliable [61]. This problem is avoided in the newer calculation of Li and Gale where each particle is given its own experimentally fitted form factor. Also in ref. [60] $\pi a_1 \to l^+l^-$ process is shown to have a large contribution to the dilepton rates at intermediate masses and is included in the rates.

To calculate the thermal yield emitted in a heavy ion collision, the production rate, dR/d^3p, has to be integrated over the total space-time volume, i.e. over all fluid cells with $T > T_f$. For photons the thermal spectrum is given by

$$E\frac{dN^\gamma}{d^3p} = \int d^4x \Big\{ \quad w(\varepsilon,\rho_{\rm B})\; E\frac{dR^{\rm QGP}}{d^3p}(p\cdot u, T, \mu_{\rm B}) + [1-w(\varepsilon,\rho_{\rm B})]\, E\frac{dR^{\rm HG}}{d^3p}(p\cdot u, T)\Big\}, \tag{3.1}$$

where $w(\epsilon,\rho_{\rm B})$ is the volume fraction of plasma. As mentioned, the rates for the hadron phase do not contain processes involving baryons. Hence, there is no dependence on $\mu_{\rm B}$. The dilepton spectrum is given by an analogous integration.

Unless otherwise mentioned, the freeze-out temperature in the following calculations has been $T_f \approx 140$ MeV in all S+Au calculations and in Pb+Pb cal-

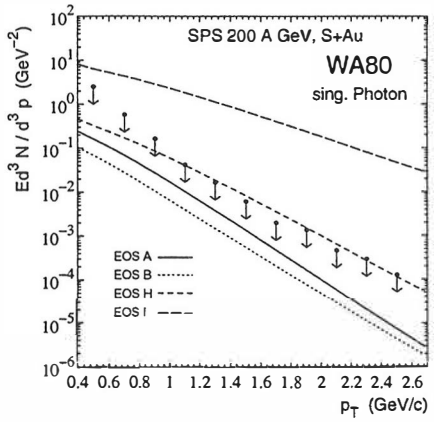

Figure 3.1: Single photon p_T spectra in S+Au collisions for the different EoSs compared with the upper bound of WA80 data [62].

culations with EoSs D and H. When EoS A is used in Pb+Pb calculations, the freeze-out temperature has been $T_f \approx 120$ MeV. The effect of the freeze-out temperature on photons and low-mass electron pairs has been discussed separately.

3.1 Photons

At the CERN SPS the thermal photon emission has been measured by the WA80 collaboration in S+Au [62] and by the WA98 collaboration in the Pb+Pb collisions [63]. In these experiments the background photon yield due to mostly π and η decays after freeze-out is extracted and the data is directly comparable to the calculated thermal yield.

The WA80 collaboration has been able to measure only an upper bound for direct photons. Nevertheless that is enough to rule out certain scenarios (see fig. 3.1). If an ideal gas EoS is assumed, the yield lies one to two orders of magnitude above the experimental upper limit[2], whereas all the other EoSs lead to yields below it. In principle the photon yield could be used to determine the value of T_c from the data, but the present experimental accuracy is not good enough for this purpose. As seen in fig. 3.1, the WA80 data rules out only high initial temperatures. To prevent the initial temperature from increasing too high, a sufficient amount of degrees of freedom is required. From this point of view it is insignificant whether these degrees of freedom are hadronic or partonic.

Similar effect of the number of degrees of freedom can be seen in the ratios of

[2]This EoS is also ruled out by the transverse momentum spectrum of negative hadrons; see paper I.

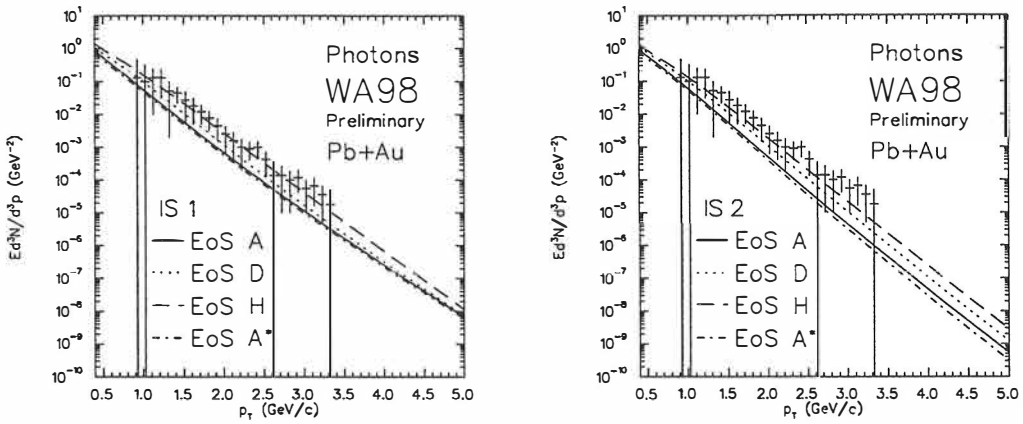

Figure 3.2: Single photon p_T spectra in Pb+Pb collisions for the different EoSs and initial states (left: IS 1, right: IS 2) compared with the preliminary data from WA98 collaboration [63]. Freeze-out temperature is $T_f \approx 140$ MeV for both EoS D and H, and $T_f \approx 120$ MeV for EoS A. EoS A* stands for the use of EoS A and $T_f \approx 140$ MeV.

the yields obtained using EoS A and EoS H. In S+Au collision EoS H leads to 8–10 times larger photon production whereas in Pb+Pb collision the corresponding factor is only 2–5 (see fig. 3.2) when IS 1 is used and the freeze-out temperature is $T_f \approx 140$ MeV for both EoSs. The main reason for this difference is that the hadronic EoSs used in papers I and IV are different as explained in section 2.2. The EoS H of paper I contains fewer hadrons than EoS H of paper IV. The extra degrees of freedom are heavier and thus suppressed by the Boltzmann factor at low temperatures, but when energy density increases, these degrees of freedom become available. This leads to a lower temperature which decreases photon production.

In S+Au collision the yield obtained using EoS H was very close to the experimental upper bound. Since the phase transition is more probable in a collision of heavier nuclei, one could expect similar behaviour in Pb+Pb collision. Quite surprisingly this is not the case. EoS H combined with IS 1 gives the best fit to the data and both IS 1 and IS 2 combined with EoS A seem to lead to too small yields. However, one has to remember that the Pb+Pb data presented by WA98 collaboration [63] are so far only preliminary and may change. Also the resolving power of the photon spectrum is at present based on overall normalisation. The difference between the yields is the above mentioned factor 2–5 which is within the present experimental errors. If the normalisation changes by a factor two, all combinations of equations of state and initial states reproduce the data.

At low values of p_T both initial states lead to similar photon production, but the larger p_T the larger difference the initial state causes. Around $p_T = 3$ GeV/c

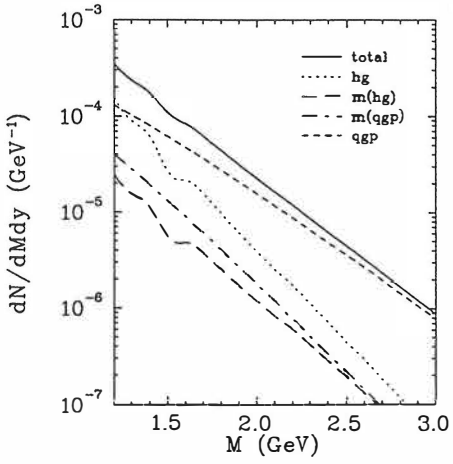

Figure 3.3: The emission of thermal electron pairs from different phases of the fireball. Equation of state is EoS D and initial state IS 1. No kinematic cuts have been applied.

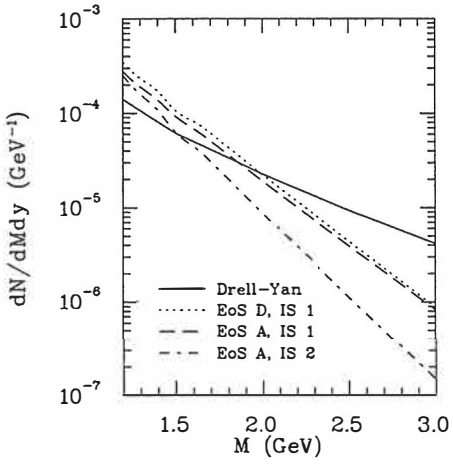

Figure 3.4: Mass distribution of thermal electron pairs in Pb+Pb collision compared with Drell-Yan pairs calculated at $y_{cm} = 0$. No kinematic cuts have been applied.

the change of the initial state changes the photon emission by a factor of 1.5–3 depending on the EoS, but the difference is much larger at larger values of p_T, which WA98 does not measure. At $p_T > 4$ GeV/c the difference is close to an order of magnitude. On the other hand, at so high values of p_T, the spectrum may be dominated by pre-equilibrium photons absent from the hydrodynamical calculation.

Thus, constraining the evolution to reproduce the measured hadron spectra does not fix the photon yield completely but leaves – at least in principle – an opportunity to differentiate experimentally between different evolution scenarios. Yet one should keep in mind the uncertainties in the rate calculations both in the QGP and a hadron gas near T_c. The results presented above are based on the considerable difference in the rates at the same temperature between perturbative QCD results [49] and leading order estimates in a hadron gas [48,51].

3.2 Intermediate mass lepton pairs

The dimuon yield at intermediate masses ($1.5 < M < 2.5$ GeV) has been measured by the NA50 collaboration [64]. In their analysis the data are roughly a factor 2 above the sum of Drell-Yan pairs and pairs from charm decays. Unfortunately it is not straightforward to compare calculations with data since the NA50 acceptance cuts are single particle cuts [65] whereas the calculations de-

scribed here give the distribution of pairs. Hence it is not possible to compare the calculated thermal yield with the experimental one without making additional assumptions of the angular distribution of single particles. The calculated thermal yield is therefore compared with Drell-Yan yield of dileptons in Pb+Pb collision without any acceptance cuts or decay contribution after freeze-out.

In fig. 3.3 the emission originating from the various phases of the fireball has been shown for EoS D and IS 1. The emission from the plasma phase dominates clearly even in this case which has a very short-lived plasma phase due to the high phase transition temperature ($T_c = 200$ MeV). Thus it is no wonder that cutting the initial temperatures by changing the initial state from IS 1 to IS 2 has a clear effect on the dilepton emission in this mass region – at 3 GeV mass the differences between IS 1 and IS 2 are close to one order of magnitude (see fig. 3.4). At so high masses the yield is, however, dominated by Drell-Yan pairs and any difference in the thermal yield is unobservable in practice. On the other hand, at lower masses ($1.5 < M < 2.0$ GeV) the thermal contribution is of the same order of magnitude than the contribution from Drell-Yan pairs and can be one source of the observed enhancement. In this mass region the dependence on the initial state is weaker but IS 1 still produces twice the amount of pairs than IS 2 independent of the EoS.

3.3 Low mass electron pairs

3.3.1 Mass spectrum

At the CERN SPS the mass spectrum of low mass ($0.2 < M < 1.5$) electron pairs has been measured by the CERES collaboration in both S+Au [66] and Pb+Pb [67] collisions. Unlike in the photon measurements by the WA98 collaboration, it is not possible to differentiate experimentally electron pairs originating from meson decays after freeze-out and thermal pairs emitted before freeze-out. To give an estimate of this background, the CERES collaboration has presented a so-called cocktail plot. This plot is based either on upscaled electron yield in p+A collisions [66,67] or more recently on thermal model calculations [68].

In the studies of this thesis, the background is estimated using the meson yields and distributions from the hydrodynamical model. However, in Pb+Pb collision the freeze-out temperature $T_f \approx 140$ MeV leads to a larger ϕ/h^- ratio than observed [70]. Thermal models [33,35] show that the system is not in complete chemical equilibrium at the time of kinetic freeze-out. Therefore the ϕ/h^- ratio is not an indication of a lower freeze-out temperature but an indication of a strangeness non-equilibrium, which the hydrodynamical model is unable to reproduce. To achieve consistency with data the ϕ yield of Pb+Pb collision is suppressed by a factor of 0.6 when $T_f \approx 140$ MeV freeze-out temperature is used. The lower freeze-out temperature of $T_f \approx 120$ MeV leads to a ϕ/h^- ratio comparable to experiment. Thus no additional factors are needed in that case.

The background in Pb+Pb collision calculated using both freeze-out temper-

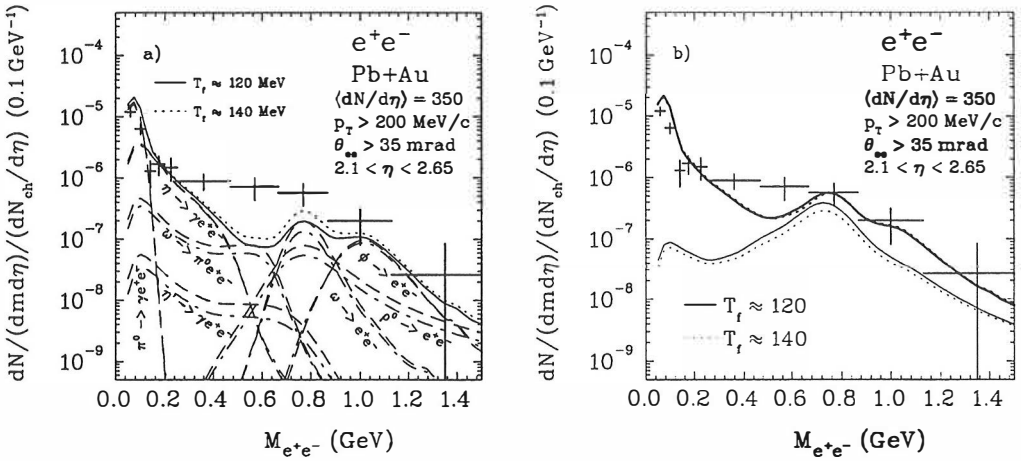

Figure 3.5: a) The estimate of the background to the thermal dielectron spectrum in Pb+Pb collisions from the meson decays after the freeze-out as calculated from the hydrodynamical result for EoS A and IS 1 using two different freeze-out temperatures. b) The thermal emission (thin lines) and total yield (thick lines) for EoS A and IS 1 in two different freeze-out temperatures. The data are preliminary and taken from ref. [69]. The kinematic cuts and detector resolution have been incorporated.

atures is shown in fig. 3.5 a). As expected the lower freeze-out temperature leads to smaller yield and the contribution from ϕ decays stays unchanged since the ϕ yield is constrained to the experimental value. At low masses the calculated background exceeds the data. This is due to the pion spectra being too flat at low values of transverse momenta as seen in fig. 2.7 for negative particles, mostly pions. Because the overall normalisation is correct, there are too many pions in the CERES acceptance region. In the fig. 2.7 one can also see the calculated π^0 p_T spectrum in S+Au collision. This spectrum is reproduced better and therefore there is no similar overshoot in the S+Au dielectron mass spectrum (see fig. 3.6 b).

If the freeze-out temperature is decreased, the lifetime of the system increases. Consequently the thermal emission increases as shown in fig. 3.5 b). However, the change in freeze-out temperature affects the background and the thermal yield in opposite ways and the total yield is almost unaffected. In the present study this means that the low mass electron pair results are insensitive to the possible uncertainty in freeze-out temperature. On the other hand, this behaviour highlights the uncertainty of the background. Since the experimental yield consists of two parts, the experimental constraints to the thermal yield are equally uncertain.

The effect of an EoS to electron pair emission in S+Au and Pb+Pb collisions

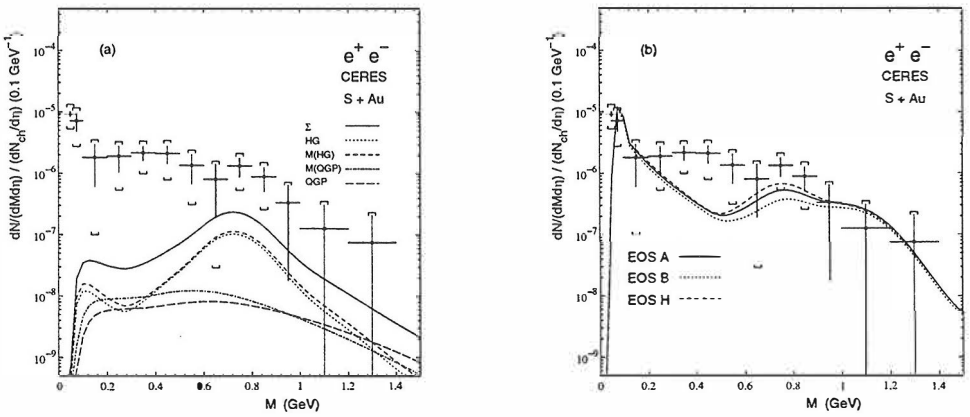

Figure 3.6: The mass spectrum of electron pairs in S+Au collision compared with the measurement of the CERES collaboration [66]. Kinematic cuts and detector resolution are incorporated. a) Contributions from different phases of the fireball for EoS A. b) Total dielectron spectrum including background for different equations of state.

is presented in figs. 3.6 b) and 3.7 a), respectively. The production rates in equally hot plasma and hadron gas differ and this difference can in principle be seen in the thermal yields. However, these differences are relatively small and when the background is added to the thermal yield, the difference due to the EoS is below a factor two in S+Au calculations and below a factor 1.3 in Pb+Pb collision. Again the different behaviour in different collisions is due to different sets of equations of state. In a hadron gas the production rate is peaked around the free ρ mass, but there is no such a structure in the production rates in the plasma phase. Thus, as seen in the figures, the longer the fireball stays in the plasma phase, the smaller the yield around the free ρ mass is. When EoS B is used, there is no hadron gas phase at all and the dielectron yield around the free ρ mass is lowest. This EoS is not used at all in the Pb+Pb calculations. Therefore comparing the dielectron yields obtained using EoSs A and H in both collisions gives a better idea how electron pair emission depends on the equation of state. In S+Au collision EoS H leads to a yield which is above the yield given by EoS A by a factor of 1.4 at largest. Since this is comparable to the factor 1.3 in Pb+Pb collision, the phase transition temperature affects emission in the same way in both collisions.

In fig. 3.7 b) the effect of an initial state to low mass electron pairs is shown. It can be seen that the effect is virtually nonexistent and begins to increase slowly at the larger masses. This kind of behaviour can be easily understood since – as shown in fig. 3.6 a) – the major contribution to the thermal yield

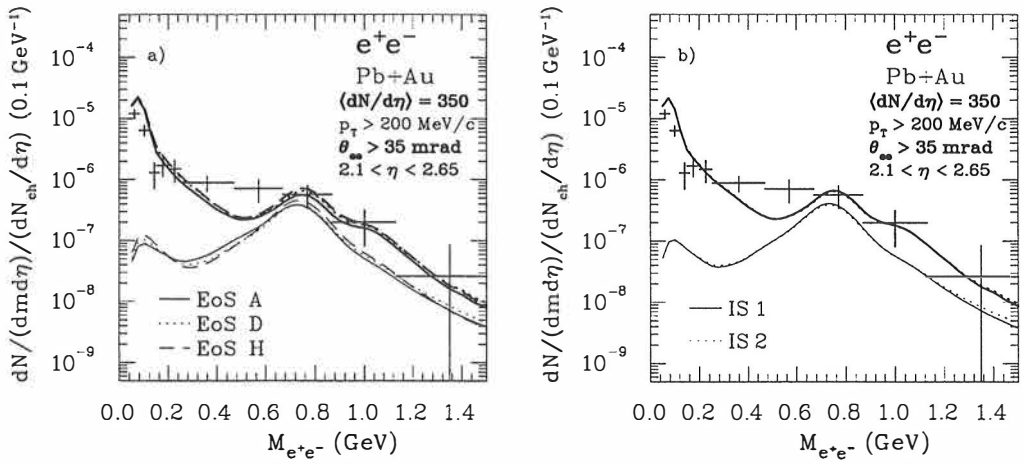

Figure 3.7: The mass spectrum of electron pairs in Pb+Pb collision compared with preliminary data from ref. [69]. Kinematic cuts and detector resolution are incorporated. a) Spectrum using three different equations of state and initial state IS 1. b) Spectrum using two different initial states and EoS D. In both panels thin lines correspond to the thermal emission and thick lines to the total yield including background.

comes from the hadronic phase of the fireball. The change in the initial state cuts the initial temperature and thus emission from the plasma phase, but the dominant hadronic phase is almost unaffected.

The result of these exercises is that when the evolution of the dense stage of an ultrarelativistic heavy-ion collision is constrained to reproduce the hadron spectra, the possible variations in the equation of state or the initial state affect the mass spectrum of low mass electron pairs surprisingly little. Similar result has been achieved earlier using a transport model [71]. However, even if this behaviour is common to both hydrodynamical and transport calculations, in general the transport calculations give larger yield than the hydrodynamic ones [72]. The cause of this discrepancy is at present unknown.

The calculations fail to reproduce the observed excess of electron pairs around $M \approx 500$ MeV. Without in-medium changes of particle properties, the other hydrodynamical models fail as well [73]. To reach the data, the thermal emission should be enhanced by a factor three in this mass region. When the data and calculations were compared in paper IV, an enhancement factor ten was needed to reproduce the data. The calculations presented here are the same but the data have changed and therefore the needed enhancement is much smaller than estimated before. The data have changed around the free ρ mass as well and it is no longer necessary to require that the modified rates do not suppress emission in that mass region.

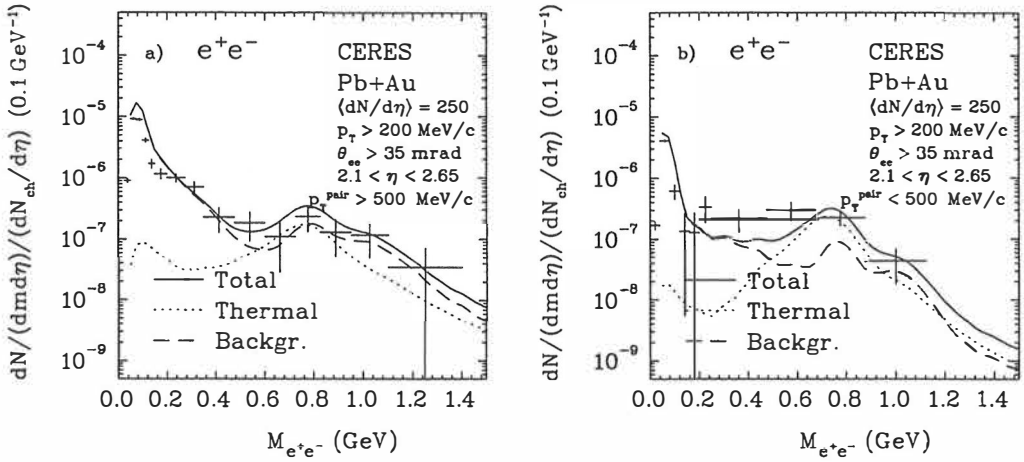

Figure 3.8: The mass spectrum of a) $p_T > 500$ MeV/c and b) $p_T < 500$ MeV/c electron pairs for EoS D and IS 2 compared with the measurement of the CERES collaboration [74]. Kinematic cuts and detector resolution are incorporated. NB The average charged particle multiplicity in the calculation is $\langle dN/d\eta \rangle = 330$.

It is worth noticing that so far the Pb+Pb results are compared with preliminary data from ref. [69] for which the average charged particle multiplicity is $\langle dN/d\eta \rangle = 350$. The Pb+Pb calculation is tuned to reproduce the results of the NA49 collaboration which uses a centrality trigger different from the trigger of the CERES experiment. Hence the calculation yields an average multiplicity of $\langle dN/d\eta \rangle = 330$ within the CERES acceptance region. The CERES collaboration finds both the shape of the spectrum and the yield scaled with multiplicity to vary with multiplicity [67]. Therefore the results should be compared with the high multiplicity data set rather than with $\langle dN/d\eta \rangle = 250$ data presented in ref. [74]. Similar precaution is not necessary when the calculated spectrum in S+Au collision is compared to the data since in that case the average experimental multiplicity is $\langle dN/d\eta \rangle = 125$ whereas the model gives $\langle dN/d\eta \rangle = 115$.

The CERES collaboration has published some hadron data at different centralities [75]. The use of this data to tune the initial conditions is not straightforward since the model presented here assumes cylindrical symmetry and is therefore applicable only to central collisions. However, if the hadron spectra are reproduced, the possible variations in the initial state affect low mass dielectron emission very little. Therefore it can be argued that neither the deviations from cylindrical symmetry would cause remarkable changes in dielectrons. In that case it would be possible to approximate the initial state formed in a non-central collision by a cylindrical one and use this model for calculating the dielectron emission at different centralities.

So far there is no data available which would have been divided into low and

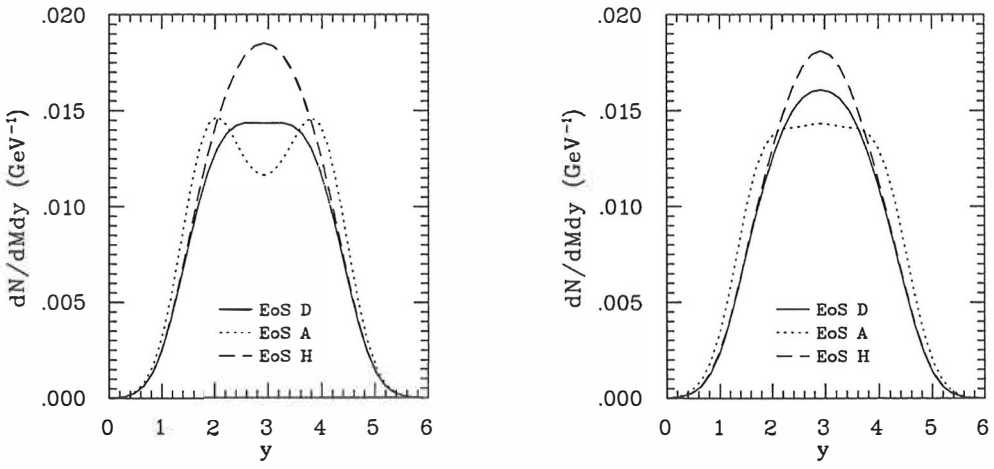

Figure 3.9: Rapidity distributions of thermal electron pairs of mass 770 MeV. Initial state is IS 1 (left) or IS 2 (right). No kinematic cuts or detector resolution has been applied.

high pair-p_T samples and for which the average multiplicity would be $\langle dN/d\eta \rangle \approx 330$. Therefore the calculated results are compared with $\langle dN/d\eta \rangle = 250$ data in fig. 3.8. The comparison has to be done with caution but one can still say that the enhancement is concentrated at low values of p_T where the calculated thermal yield is not large enough to fill the gap between the data and the background whereas at large p_T the small enhancement is explained by the thermal contribution without any in-medium modifications in the rates.

3.3.2 Rapidity spectrum

In the previous sections it was shown that the phase transition temperature affects the dilepton mass spectrum only little. The effect on photon p_T spectra is larger but the phase transition temperature affects mostly the normalisation of the spectrum – the change in the temperature scales the yield up or down. In contrast to this, the shape of the rapidity distribution of dileptons shows a strong dependence on phase transition temperature at masses around 770 MeV, i.e. free ρ mass. Unfortunately the shape of this distribution is equally sensitive to the initial velocity profile too (see fig. 3.9).

The interesting double peaked shape is not due to some structure in the dilepton production rates but is a result of sufficiently hot, long living and fast moving parts of the fireball, i.e. long living mixed phase. The entire lifetime of the fireball and the mixed phase is almost similar for both initial states, but since the initial velocity profile is flatter in the case of IS 2, the lifetime in the middle of the fireball is longer. Consequently the emission in mid rapidities is

larger and the gap between the two peaks of the spectrum is filled. Thus the shape of the final spectrum is a result of a complicated interplay between the initial velocities and subsequent evolution.

If production rates including in-medium modifications are used, the shape still shows dependence on T_c at 770 MeV mass, but the signal may be even clearer at lower values of mass. For example, when the rates calculated by Rapp et al. [76] are used, the signal is most prominent around 500 MeV mass. Thus, the rapidity spectrum could be useful also in differentiating between different scenarios concerning the in-medium properties of vector mesons. In view of these results it is regrettable that no existing nor planned experiment is capable of measuring the rapidity spectrum of dileptons but their acceptance is reduced to a rather narrow rapidity window.

Chapter 4

Outlook

Hydrodynamics has its drawbacks in describing ultrarelativistic heavy-ion collisions. The underlying assumptions are bold and there are phenomena it cannot describe even in principle. Nevertheless, hydrodynamical models are the only ones where the phase transition can be included in the evolution and various equations of state tested explicitly. The effects of rehadronisation can thus be studied even if the details of the microscopic processes are not known. Also, even if the assumptions are bold, they are clear and easy to understand. Hydrodynamical models are as well relatively simple and give an intuitively transparent picture of the evolution of the dense stage.

A major problem in applying hydrodynamics to describe heavy-ion collisions is how to choose the initial conditions for the hydrodynamical evolution. In this thesis a parametrisation for the initial state was developed. This parametrisation was constrained by requiring that the subsequent evolution reproduces the observed hardonic spectra and that the parametrisation has to be applicable in all nucleus-nucleus collisions at the CERN SPS energy. It turned out that these requirements constrain the equation of state only by stating that it has to have a sufficient number of degrees of freedom. The effects of a possible phase transition to the evolution can be removed by changing the initial state. There is also some freedom in choosing the appropriate initial density and velocity distributions for each equation of state, although their combinations have to be chosen very carefully to reproduce the hadron spectra.

After fixing the initial conditions to reproduce the hadron data, lepton pairs and photons emitted in each evolution scenario were calculated and their dependence on the equation of state and initial distributions was studied. It was found that electromagnetic probes do not give an easy and clear method to discriminate between different scenarios. Instead of measuring one signal, one has to measure many of them to be able to give further constraints. Of the electromagnetic probes considered in this thesis, the photon yield seems to have the strongest potential to constrain the phase transition temperature. This, however, requires the experimental accuracy to increase. The comparison of calculations to the present, preliminary WA98 data gave fascinating results and it will be

interesting to see what the final data look like.

The intermediate mass dileptons were found to be sensitive to the maximum energy density i.e. the maximum temperature reached in the collision. However, in this mass region the thermal yield competes with Drell-Yan pairs and pairs from charm decays. To be able to unambiguously use the thermal yield as a thermometer of the collision, one should be able to separate these contributions.

The relative insensitivity of low mass electron pairs to the initial state and phase transition temperature means that the observed excess measured by the CERES collaboration is due to the properties of lepton production in the dense matter, not to some exotic evolution scenario. This makes the testing of the various proposed in-medium modified rates easier since it is enough to constrain the evolution to reproduce the hadron spectra. From this point of view the closer details of the evolution are insignificant. On the other hand, the rapidity spectrum of $M = 770$ MeV electron pairs turned out to be very sensitive to the development of flow during the evolution and it would be interesting to compare this result with experimental data.

In the future RHIC and LHC experiments the available c.m. energy will be a factor of 12 and 330 larger than in the present SPS experiments. It has been estimated that if the system thermalises, this would lead to initial temperatures of 450 and 1000 MeV, respectively [5]. Both values are well beyond the critical temperature. Thus, if the system is thermalised, the evolution of the dense stage is affected by the properties of the plasma phase and its rehadronisation. Since hydrodynamical models are the only ones where the phase transition can be included in the description they will be very useful in modelling collisions in both RHIC and LHC energies.

As the collision energy increases it becomes possible to use the methods of perturbative QCD to calculate particle production in the primary collision. At RHIC energy there is still a sizable non-perturbative component present but at the LHC energy the initial energy densities can be estimated perturbatively. This gives a more reliable starting point for the hydrodynamical evolution. To give predictions of transverse energy and particle multiplicities in LHC/ALICE, the work to modify the hydrodynamical model of this thesis to be practically applicable at LHC energies and to calculate the initial conditions using perturbative QCD has already been initiated.

References

[I] Publication I of this thesis.

[II] Publication II of this thesis.

[III] Publication III of this thesis.

[IV] Publication IV of this thesis.

[1] N. Cabibbo and G. Parisi, Phys. Lett. **59B**, 67 (1975); J.C. Collins and M.J. Perry, Phys. Rev. Lett. **34**, 1353 (1975).

[2] E. Laermann, Nucl. Phys. Proc. Suppl. **63**, 114 (1998).

[3] K. Olive, Nucl. Phys. **B190**, 483 (1981).

[4] N. Itoh, Prog. Theor. Phys. **44**, 291 (1970).

[5] J. Stachel, Proc. of INPC 98, Paris, Aug 24-28, 1998; to be published in Nucl. Phys. **A.** (nucl-ex/9903007).

[6] L.D. Landau, Izv. Akad. Nauk. SSSR 17, 51 (1953).

[7] D. Rischke, To be published in the proceedings of 11th Chris Engelbrecht Summer School in Theoretical Physics: Hadrons in Dense Matter and Hadrosynthesis, Cape Town, South Africa, 4-13 Feb 1998 (nucl-th/9809044).

[8] J.P. Boris and D.L. Book, J. Comp. Phys. **11**, 38 (1973); D.L. Book, J.P. Boris and K. Hain, J. Comp. Phys. **18**, 248 (1975); J.P Boris and D.L. Book, J. Comp. Phys. **20**, 397 (1976).

[9] M. Kataja, Z. Phys. C **38**, 419 (1988).

[10] S.T. Zalesak, J. Comp. Phys. **31**, 335 (1979).

[11] H. von Gersdorff, L. McLerran, M. Kataja and P.V. Ruuskanen, Phys. Rev. D **34**, 794 (1986).

[12] P. Huovinen, M.Sc. thesis, University of Jyväskylä, 1996.

[13] G. Welke, R. Venugopalan and M. Prakash, Phys. Lett. **245B**, 137 (1990); R. Venugopalan and M. Prakash, Nucl. Phys. **A546**, 245 (1992).

[14] J. Alam, S. Raha and B. Sinha, Phys. Rep. **273**, 243 (1996).

[15] C.M. Hung and E. Shuryak, Phys. Rev. C **57**, 1891 (1998).

[16] E. Laermann, Nucl. Phys. **A610**, 1 (1996).

[17] S.A. Bass, M. Gyulassy, H. Stöcker and W. Greiner, J. Phys. G **25**, R1 (1999).

[18] F.R Brown *et al.*, Phys. Rev. Lett. **65**, 2491 (1990).

[19] Particle Data Group, Phys. Rev. D **50**, 1173 (1994).

[20] J.D. Bjorken, Phys. Rev. D **27**, 140 (1983).

[21] B.R. Schlei, D. Strottman and N. Xu, Phys. Rev. Lett. **80**, 3467 (1998).

[22] J. Boltz, U. Ornik and R.M. Weiner, Phys. Rev. C **46**, 2047 (1992).

[23] A. Bohr and B.R. Mottelson, *Nuclear Structure*, Vol. 1, (W.A. Benjamin,Inc, New York, 1969).

[24] J. Bächler *et al.* (NA35 collaboration), Phys. Rev. Lett. **72**, 1419 (1994).

[25] M. Gaździcki *et al.* (NA35 collaboration), Nucl. Phys. **A590**, 197c (1995).

[26] P.G. Jones *et al.* (NA49 collaboration), Nucl. Phys. **A610**, 188c (1996).

[27] D. Röhrich *et al.* (NA35 collaboration), Nucl. Phys. **A566**, 35c (1994).

[28] M. Murray *et al.* (NA44 collaboration), in *Strangeness '95*, AIP Conference Proceedings **340**, edited by J. Rafelski, (AIP Press, 1995), p. 162.

[29] P. Jacobs *et al.* (NA49 collaboration), Proceedings of the *Int. Conference on the Physics and Astrophysics of the Quark-Gluon Plasma*, (Jaipur/India March 1997) edited by B.C. Sinha, D.K. Srivastava and Y.P. Viyogi.

[30] R. Santo *et al.* (WA80 collaboration), Nucl. Phys. **A566**, 61c (1994).

[31] T. Alber *et al.* (NA35 collaboration), Z. Phys. C **64**, 195 (1994).

[32] H. Appelshäuser *et al.* (NA49 collaboration), Phys. Rev. Lett. **82**, 2471 (1999).

[33] F. Becattini, M. Gaździcki and J. Sollfrank, Eur. Phys. J. C **5**, 143 (1998).

[34] C.M. Hung and E. Shuryak, Phys. Rev. C **57**, 1891 (1998).

[35] P. Braun-Munzinger, J. Stachel, J.P. Wessels and N. Xu, Phys. Lett. **365B**, 1 (1996).

[36] J. Cleymans and K. Redlich, Phys. Rev. Lett. **81**, 5284 (1998).

[37] F. Grassi, Y. Hama and T. Kodama, Phys. Lett. **355B**, 5 (1995).

[38] F. Cooper and G. Frye, Phys. Rev. D **10**, 186 (1974).

[39] K.A. Bugaev, Nucl. Phys. **A606**, 559 (1996).

[40] Cs. Anderlik, L.P. Csernai, F. Grassi, W. Greiner, Y. Hama, T. Kodama, Zs.I. Lazar, V. Magas, H. Stöcker, preprint IFUSP-P-1310 (nucl-th/9806004).

[41] J. Sollfrank, P. Koch, and U. Heinz, Z. Phys. C **52**, 593 (1991).

[42] J.L. Goity and H. Leutwyler, Phys. Lett. **228B**, 517 (1989); M. Prakash, M. Prakash, R. Venugopalan and G. Welke, Phys. Rep. **227**, 323 (1993).

[43] B. Kämpfer, preprint FZR-149 (hep-ph/9612336).

[44] U.A. Wiedemann, B. Tomášik and U. Heinz, Nucl. Phys. **A638**, 475c (1998).

[45] H. Appelshäuser *et al.* (NA49 collaboration), Eur. Phys. J. C **2**, 661 (1998).

[46] B.R. Schlei, D. Strottman, J.P. Sullivan and H.W. van Hecke, preprint LA-UR-98-4184 (nucl-th/9809070).

[47] M.M. Aggarwal *et al.* (WA98 Collaboration), preprint IKP-MS-990102 (nucl-ex/9901099).

[48] J. Kapusta, P. Lichard, and D. Seibert, Phys. Rev. C **44**, 2774 (1991).

[49] C. Traxler, H. Vija, and M. Thoma, Phys. Lett. **346B**, 329 (1995).

[50] H. Nadeau, J. Kapusta, and P. Lichard, Phys. Rev. C **45**, 3034 (1992); Phys. Rev. C **47**, 2426 (1993).

[51] L. Xiong, E. Shuryak, and G.E. Brown, Phys. Rev. D **46**, 3798 (1992).

[52] P. Lichard and M. Prakash (unpublished).

[53] J. Cleymans, J. Fingberg, and K. Redlich, Phys. Rev. D **35**, 2153 (1987).

[54] E. Braaten, R.D. Pisarski and T.-C. Yuan, Phys. Rev. Lett. **64**, 2242 (1990).

[55] T. Altherr and P.V. Ruuskanen, Nucl. Phys. **B380**, 377 (1992).

[56] See e.g., Quark Matter'97, Nucl. Phys. **A638**, (1998).

[57] J. Wambach and R. Rapp, Nucl. Phys. **A638**, 171c (1998).

[58] P. Huovinen and M. Prakash, Phys. Lett. **450B**, 15 (1999).

[59] C. Gale and P. Lichard Phys. Rev. D **49**, 3338 (1994).

[60] G.Q. Li and C. Gale, Phys. Rev. C **58**, 2914 (1998).

[61] C. Gale, private communication.

[62] R. Albrecht *et al.* (WA80 collaboration), Phys. Rev. Lett. **76**, 3506 (1996)

[63] V. Manko, Int. Nucl. Phys. Conf. (INPC-98), August '98, Paris, France. The data is extracted from nucl-th/9812006 by S. Sarkar, P. Roy, J. Alam and B. Sinha.

[64] E. Scomparin *et al.* (NA50 Collaboration), Nucl. Phys. **A610**, 331c (1996).

[65] C. Lourenço, private communication.

[66] G. Agakichiev *et al.* (CERES collaboration), Phys. Rev. Lett. **75**, 1272 (1995).

[67] G. Agakichiev *et al.* (CERES Collaboration), Phys. Lett. **422B**, 405 (1998).

[68] I. Tserruya, ECT* workshop, Trento, March 15-26, 1999.

[69] B. Lenkeit, Doctoral Thesis, University of Heidelberg, 1998.

[70] V. Friese *et al.* (NA49 Collaboration) J. Phys. G **23**, 1837 (1997).

[71] V. Koch and C. Song, Phys. Rev. C **54**, 1903 (1996).

[72] R. Rapp, ECT* workshop, Trento, March 15-26, 1999.

[73] A. Drees, Nucl. Phys. **A610**, 536c (1996).

[74] B. Lenkeit, Proc. of INPC 98, Paris, Aug 24-28, 1998; to be published in Nucl. Phys. **A.**

[75] F. Ceretto *et al.* (CERES collaboration), Nucl. Phys. **A638**, 467 (1998).

[76] R. Rapp, M. Urban, M. Buballa, and J. Wambach, Phys. Lett. **417B**, 1 (1998).

[77] K.J. Eskola, K. Kajantie and P.V. Ruuskanen, Eur. Phys. J. C **1**, 627 (1998).